Supporting Information for

Analysis of bipolar membranes for electrochemical CO_2 capture from air and oceanwater

Justin C. Bui[1,2], Éowyn Lucas[3,4], Eric W. Lees[2], Andrew K. Liu[1,2], Harry A. Atwater[3,4], Chengxiang Xiang[3], Alexis T. Bell[1,2], & Adam Z. Weber[2]*

[1] Department of Chemical and Biomolecular Engineering
University of California Berkeley
Berkeley, CA 94720, USA

[2] Liquid Sunlight Alliance
Lawrence Berkeley National Laboratory
Berkeley, CA 94720, USA

[3] Liquid Sunlight Alliance
California Institute of Technology
Pasadena, CA 91125, USA

[4] Department of Applied Physics
California Institute of Technology
Pasadena, CA 91125, USA

Corresponding Author: azweber@lbl.gov
Phone: (510) 486-6308

Contents

S1. Computational Methods

S1.1 Macroscopic Equilibrium Calculation

Each homogeneous reaction should maintain macroscopic equilibrium, even considering the Second Wien Effect. The derivation below is shown for bicarbonate dissociation, but similar derivations can be constructed for all reactions impacted by an electric field.

$$\mu_{H^+} + \mu_{CO_3^{2-}} = \mu_{HCO_3^-} + \mu_{H_2O} \tag{S1}$$

For each species the chemical potential can be written as follows:

$$\mu_{H^+} = \mu_{H^+}^0 + RT\ln(a_{H^+}) + F\Phi \tag{S2}$$

$$\mu_{CO_3^{2-}} = \mu_{CO_3^{2-}}^0 + RTln\left(a_{CO_3^{2-}}\right) - 2F\Phi \tag{S3}$$

$$\mu_{HCO_3^-} = \mu_{HCO_3^-}^0 + RTln\left(a_{HCO_3^-}\right) - F\Phi \tag{S4}$$

$$\mu_{H_2O} = \mu_{H_2O}^0 + RTln\left(a_{H_2O}\right) \tag{S5}$$

We apply the equations for activity for the ions and assume that water activity in the polymer is unity because the polymer is in contact with liquid water.

$$\mu_{H^+} = \mu_{H^+}^0 + RT\ln\left(\frac{c_{H^+}c_{H_2O}^0}{c_{H_2O}c_{H^+}^0}\right) - \frac{1}{2}RT\ln(f(E)) + F\Phi \tag{S6}$$

$$\mu_{CO_3^{2-}} = \mu_{CO_3^{2-}}^0 + RT\ln\left(\frac{c_{CO_3^{2-}}c_{H_2O}^0}{c_{H_2O}c_{CO_3^{2-}}^0}\right) - RT\ln(f(E)) - 2F\Phi \tag{S7}$$

$$\mu_{HCO_3^-} = \mu_{HCO_3^-}^0 + RT\ln\left(\frac{c_{HCO_3^-}c_{H_2O}^0}{c_{H_2O}c_{HCO_3^-}^0}\right) - \frac{1}{2}RT\ln(f(E)) - F\Phi \tag{S8}$$

$$\mu_{H_2O} = \mu_{H_2O}^0 \tag{S9}$$

Substituting equations (S6)-(S9) into equation (S1) yields the following:

$$\mu_{H^+}^0 + RT\ln\left(\frac{c_{H^+}c_{H_2O}^0}{c_{H_2O}c_{H^+}^0}\right) + \mu_{CO_3^{2-}}^0 + RT\ln\left(\frac{c_{CO_3^{2-}}c_{H_2O}^0}{c_{H_2O}c_{CO_3^{2-}}^0}\right) - RT\ln(f(E)) = \mu_{HCO_3^-}^0 + RT\ln\left(\frac{c_{HCO_3^-}c_{H_2O}^0}{c_{H_2O}c_{HCO_3^-}^0}\right) + \mu_{H_2O}^0 \quad \text{(S10)}$$

Rearranging:

$$\mu_{H^+}^0 + \mu_{CO_3^{2-}}^0 - \mu_{HCO_3^-}^0 - \mu_{H_2O}^0 = -RT\ln\left(\frac{c_{CO_3^{2-}}c_{H_2O}^0}{c_{H_2O}c_{CO_3^{2-}}^0}\frac{c_{H^+}c_{H_2O}^0}{c_{H_2O}c_{H^+}^0}\frac{c_{H_2O}c_{HCO_3^-}^0}{c_{HCO_3^-}c_{H_2O}^0}\right) + RT\ln(f(E)) \quad \text{(S11)}$$

$$\frac{1}{RT}\left(\mu_{HCO_3^-}^0 + \mu_{H_2O}^0 - \mu_{H^+}^0 - \mu_{CO_3^{2-}}^0\right) + \ln\left(\frac{c_{CO_3^{2-}}^0 c_{H^+}^0}{c_{HCO_3^-}^0}\right) = \ln\left(\frac{c_{CO_3^{2-}}c_{H_2O}^0}{c_{H_2O}}\frac{c_{H^+}c_{H_2O}^0}{c_{H_2O}}\frac{c_{H_2O}}{c_{HCO_3^-}c_{H_2O}^0}\right) - \ln(f(E)) \quad \text{(S12)}$$

Exponentiate both sides:

$$f(E)\left(\frac{c_{CO_3^{2-}}^0 c_{H^+}^0}{c_{HCO_3^-}^0}\right)\exp\left(\frac{\mu_{HCO_3^-}^0 + \mu_{H_2O}^0 - \mu_{H^+}^0 - \mu_{CO_3^{2-}}^0}{RT}\right) = \left(\frac{c_{CO_3^{2-}}c_{H_2O}^0}{c_{H_2O}}\frac{c_{H^+}c_{H_2O}^0}{c_{H_2O}}\frac{c_{H_2O}}{c_{HCO_3^-}c_{H_2O}^0}\right) \quad \text{(S13)}$$

Lastly, we recognize the following relationship:

$$\left(\frac{c_{CO_3^{2-}}^0 c_{H^+}^0}{c_{HCO_3^-}^0}\right)\exp\left(\frac{\mu_{HCO_3^-}^0 + \mu_{H_2O}^0 - \mu_{H^+}^0 - \mu_{CO_3^{2-}}^0}{RT}\right) = K_2(E=0) \quad \text{(S14)}$$

where $K_2(E=0)$ is the macroscopic equilibrium constant under no electric field.

Finally, this provides the final expression of macroscopic equilibrium, consistent with the kinetic description that an increased electric field results in the shifting of the equilibrium towards the dissociation products:

$$K_2(E=0)f(E) = \left(\frac{c_{CO_3^{2-}} c^0_{H_2O}}{c_{H_2O}} \frac{c_{H^+} c^0_{H_2O}}{c_{H_2O}} \frac{c_{H_2O}}{c_{HCO_3^-} c^0_{H_2O}}\right) \tag{S15}$$

Essentially, the above expression says that the macroscopic equilibrium is affected by the Second Wien Effect by the defined electric-field dependence, $f(E)$, and this equilibrium holds within the interstitial volume of the polymer, because the ratio $\frac{c^0_{H_2O}}{c_{H_2O}}$ is simply the water volume fraction in the given domain.

S1.2 Thermodynamic Potential and Kinetic Potential of the BPM Junction

To determine the thermodynamic potential of a BPM junction, we can first start with the definition of Donnan potential across the CEL and AEL.

$$c_i^{CEL} = c_i^{AEL} \frac{c_{H_2O}^{CEL}}{c_{H_2O}^{AEL}} \exp\left(\frac{-z_i F \Delta\Phi_{\text{thermo}}}{RT}\right) \tag{S16}$$

Expressing the Donnan potential for protons as the species of interest:

$$\frac{c_{H^+}^{CEL}}{c_{H_2O}^{CEL}} = \frac{c_{H^+}^{AEL}}{c_{H_2O}^{AEL}} \exp\left(\frac{-F\Delta\Phi_{\text{thermo}}}{RT}\right) \tag{S17}$$

Next, we multiply both sides of the equation molar concentration of pure water, divide by a reference concentration of 1 M, and substitute in the expression for water volume fraction ($\varepsilon_w^{CEM} = \frac{c_{H_2O}^{CEM}}{c^0_{H_2O}}$, $\varepsilon_w^{AEL} = \frac{c_{H_2O}^{AEL}}{c^0_{H_2O}}$) and rearrange.

$$\frac{c_{H^+}^{AEL}}{\varepsilon_w^{CEL} c_{ref}} = \frac{c_{H^+}^{AEL}}{\varepsilon_w^{AEL} c_{ref}} \exp\left(\frac{-F\Delta\Phi_{\text{thermo}}}{RT}\right) \tag{S18}$$

We now take the negative logarithm of both sides and simplify further, recognizing that $\frac{c_{H^+}^{CEL}}{\varepsilon_w^{CEL} c_{ref}}$ and $\frac{c_{H^+}^{AEL}}{\varepsilon_w^{AEL} c_{ref}}$ represent the proton activity in the CEL and AEL, respectively:

$$-\log\left(a_{H^+}^{CEL}\right) = -\log\left(a_{H^+}^{AEL}\right) - \left(\frac{F\Delta\Phi_{\text{thermo}}}{RT}\right) \tag{S19}$$

Substituting in the definition of pH yields the following result for the thermodynamic potential across the BPM junction, which is entirely Nernstian.

$$\Delta\Phi_{\text{thermo}} = -0.059(\text{pH}_{\text{AEL}} - \text{pH}_{\text{CEL}}) \tag{S20}$$

Thus, deviations from Nernstian behavior (*i.e.,* potential drop across the junction exceeding the Nernstian potential loss) across the BPM CL are treated, in this work, as non-equilibrium kinetic overpotentials for WD.

$$\Delta\Phi_{\text{kinetic}} = \Delta\Phi_{\text{CL}} - 0.059(\text{pH}_{\text{AEL}} - \text{pH}_{\text{CEL}}) \tag{S21}$$

where, $\Delta\Phi_{\text{CL}}$ is the simulated potential drop across the CL and is described as

$$\Delta\Phi_{\text{CL}} = (\Phi_{\text{AEL|CL}} - \Phi_{\text{CL|CEL}}) \tag{S22}$$

S1.3 Detailed Discussion of Electric-Field Dependence

Rate constants for the above reactions are found in **Table S1**. As shown by Onsager[1], the equilibria of reactions that generate net charge are affected by the Second Wien Effect[2,3]

$$f(E) = \frac{K_n(E)}{K_n(E=0)} = \frac{\left(\sum_{m=0}^{\infty} \frac{1}{m!(m+1)!}(2\beta E)^m\right) \cosh(\tau\beta E) \cosh(\tau)^{\beta E}}{1+\frac{1-\exp\left(-\frac{1}{\sigma}\right)}{2}\left(\sigma^2\beta E + (4.97\sigma)\frac{\sinh(0.0835\sigma\beta E)}{\cosh^2(0.0835\sigma\beta E)}\right)}. \quad \text{(S23)}$$

where E is local electric field, and τ is a lumped parameter.

$$\tau = -0.128\ln(\cosh(0.235\sigma)) + 5.72\sigma^2, \quad \text{(S24)}$$

where σ is dimensionless number defined by the ratio of the bond dissociation length and the Bjerrum length.[4]

$$\sigma = \frac{0.58\text{ nm}}{2l_b}, l_b = \frac{eF}{8\pi\varepsilon_{H_2O}RT} \quad \text{(S25)}$$

β is a lumped parameter with units of inverse electric field defined as follows:

$$\beta E = \alpha_{\mathrm{WD}} \frac{l_b F}{RT} E. \quad \text{(S26)}$$

The value of α_{WD} in the dimensionless electric field is a fitting parameter dictates the sensitivity of the WD kinetics to the field.[3]

S1.4 Supplementary Notes on Electric-Field-Enhanced Water-Dissociation Catalyst-Layer Model

Because the focus of this work is not on the water-dissociation-catalyst behavior, we choose not to adopt a complete framework of the surface species present in the water dissociation catalyst as in our prior work[2] to ease convergence of the stiff buffer kinetics. Instead, we choose to model the WD catalyst layer as a thin neutral region in between the two ion-exchange layers, where simply the large field in between the layers drives the dissociation of water by shifting equilibrium as per Equation (S23). The thickness of the

catalyst layer, and the electric field sensitivity parameter discussed above are used to fit the WD behavior and match the electrochemical behavior to what is observed experimentally. Such an approach has been shown to represent adequately the ion transfer and electrochemical behavior of BPMs.[5,6] Analogously, this approach is similar to the use of Butler-Volmer kinetics to model current-voltage characteristics at heterogeneous electrocatalysts, as it ignores double-layer structure and proton-electron transfer kinetics in favor of a lumped analytical approach. It is important to note that the fitted thickness of the catalyst layer in the simulations is merely an effective thickness of the high-field region in the BPM CL. Recent studies have shown that even for micron-thick BPM CLs, only a small, nanometer-scale region of the CL is active for WD.[2,7] Therefore, for computational simplicity, the present model describes the high-field region as a neutral layer between the AEL and CEL, for which the effective thickness matches that of the active region in a typical BPM WD CL. While this representation does not give a complete picture of the WD catalyst, beyond its current-voltage and ionic transport characteristics, a mechanistic picture of WD is irrelevant to the crux of this work, which focuses on carbon species management and *in situ* CO_2 generation in the CEL.

S1.5 Supplementary Expressions for Modeling Transport

In the electrolyte phase diffusion coefficients are set to their values in water (**Table S1**), but in the BPM, they are corrected by the following relationship:[6,8]

$$D_{i,eff} = \frac{\phi_L^q D_{i,w}}{x_w(1+\frac{1}{\lambda}\zeta_i)}, \tag{S27}$$

In this framework, q is a fitting parameter related to the tortuosity of the ionomer and x_w is the ratio of the moles of water in the membrane to the sum of the moles of water and fixed-charge groups given by

$$x_w = \frac{\lambda}{1+\lambda}, \tag{S28}$$

where λ is the water content of the BPM defined as the ratio of water molecules absorbed in the BPM to fixed charge groups. ϕ_L is the water volume fraction in the ionomer,

$$\phi_L = \frac{\lambda V_w}{\lambda V_w + V_M}, \tag{S29}$$

where V_w and V_M are the molar volumes of pure water and membrane, respectively. ζ_i describes the ratio of the species-water and species-membrane diffusivities,[9]

$$\zeta_i = \frac{D_{i,w}}{D_{i,M}} = \left(\frac{V_M}{V_w}\right)^{\frac{2}{3}}\left(\frac{M_{i,M}}{M_{i,w}}\right)^{\frac{1}{2}}, \tag{S30}$$

where $M_{i,M} = \left(\frac{1}{M_i}+\frac{1}{M_M}\right)^{-1}$ is the reduced molar mass.

Water transport is not directly modeled in this work, as it has been shown that water-transport limitations in BPMs do not occur until current densities > 600 mA cm^{-2}, which is beyond the range of current densities studied in the present work.[10–12] Thus, water activity is assumed to be unity, and the membrane channels are fully liquid-filled. In this scenario, water content, λ, is only a function of the local ionic environment.[13]

$$\lambda_{CEL} = (1 - f_{\mathrm{H}^+})\,\lambda_{CEL,f_{\mathrm{H}^+}=0} + f_{\mathrm{H}^+}\lambda_{CEL,f_{\mathrm{H}^+}=1} \quad \text{(S31)}$$

$$\lambda_{AEL} = (1 - f_{\mathrm{OH}^-})\lambda_{AEL,f_{\mathrm{OH}^-}=0} + f_{\mathrm{OH}^-}\lambda_{AEL,f_{\mathrm{OH}^-}=1} \quad \text{(S32)}$$

where f_{H^+} and f_{OH^-} are the fraction of ion-exchange groups in the CEL or AEL, respectively, exchanged with protons or hydroxides. $\lambda_{CEL,f_{\mathrm{H}^+}=0}$, $\lambda_{CEL,f_{\mathrm{H}^+}=1}$, $\lambda_{AEL,f_{OH^-}=0}$, $\lambda_{AEL,f_{OH^-}=1}$ are the water contents of CELs or AELs fully exchanged with protons/hydroxides or counterions.[6] The water concentration in the domain is thus defined with the following hyperbolic tangent (invoked to smooth out the boundary gradients at the membrane and electrolyte interface to encourage simulation convergence).[6] To fit the water-dissociation kinetics, it was found to be necessary to include a volume fraction term only within the porous WD CL, which multiplies the water concentration by a factor of $\varepsilon_{l,CL} = 0.253$ to account for the pore volume in the WD CL.

If $|x| < \frac{L_{CL}}{2}$ (within porous catalyst layer):

$$c_{H_2O}(x) = \varepsilon_{l,CL}\left[\frac{c^0_{H_2O}}{2}\left(2 - \tanh\left(\frac{x - x_1}{L_{char}}\right) + \tanh\left(\frac{x - x_4}{L_{char}}\right)\right) + \frac{\lambda c_M(x)}{2}\left(\tanh\left(\frac{x - x_1}{L_{char}}\right) - \tanh\left(\frac{x - x_4}{L_{char}}\right)\right)\right] \quad \text{(S33)}$$

Otherwise:

$$c_{H_2O}(x) = \frac{c^0_{H_2O}}{2}\left(2 - \tanh\left(\frac{x - x_1}{L_{char}}\right) + \tanh\left(\frac{x - x_4}{L_{char}}\right)\right) + \frac{\lambda c_M(x)}{2}\left(\tanh\left(\frac{x - x_1}{L_{char}}\right) - \tanh\left(\frac{x - x_4}{L_{char}}\right)\right)$$

In the above expression, x_1 is the leftmost position of the CEL, x_2 is the right most position of CEL, x_3 is the leftmost position of AEL, and x_4 is the rightmost position of the AEL. The characteristic length used in this study is $L_{char} = 0.58$ nm, related to the bond separation distance of water.[4] Essentially, the distribution is 55.56 M in the liquid

electrolyte domains, and governed by the local water content, λ, in the BPM domains. $c_M(x)$ is the fixed-charge concentration of the BPM, defined by the following hyperbolic tangent:

$$c_M(x) = \frac{\rho_{M,wet} \times IEC}{2}\left(\tanh\left(\frac{x-x_3}{L_{char}}\right) - \tanh\left(\frac{x-x_4}{L_{char}}\right) + \tanh\left(\frac{x-x_2}{L_{char}}\right) - \tanh\left(\frac{x-x_1}{L_{char}}\right)\right) \quad \text{(S34)}$$

where $\rho_{M,wet}$ and IEC are the wet membrane density and ion-exchange capacity, respectively. This distribution is equal to zero in the liquid electrolyte domains and represents negative and positive fixed-charge in the CEL and AEL domains, respectively. Dielectric permittivity is defined as follows for the BPM domains.[4]

$$\varepsilon = \left(\frac{c_{H_2O}}{c^0_{H_2O}}\varepsilon^{-1}_{H_2O} + \varepsilon_M^{-1}\left(1 - \frac{c_{H_2O}}{c^0_{H_2O}}\right) + \varepsilon_3^{-1}\right)^{-1}, \quad \text{(S35)}$$

where ε_M is the permittivity of the pure dioxane and ε_3 accounts for water-ionomer interactions.

$$\varepsilon_3 = \varepsilon_0\left(\frac{2.42\left(1-\frac{c^M_{H_2O}}{c^0_{H_2O}}\right)\frac{c^M_{H_2O}}{c^0_{H_2O}}}{-0.48\left(1-\frac{c^M_{H_2O}}{c^0_{H_2O}}\right)-5.03\frac{c^M_{H_2O}}{c^0_{H_2O}}} + 0.066\left(1-\frac{c^M_{H_2O}}{c^0_{H_2O}}\right)\frac{c^M_{H_2O}}{c^0_{H_2O}}\right)^{-1} \quad \text{(S36)}$$

S1.6 Boundary-Layer-Thickness Calculation

To determine the boundary-layer thickness, a simple calculation was employed. Because it was observed that bubbling occurred at approximately 20 mA cm^{-2} in the 1 M $KHCO_3$ electrolyte, which has a bulk CO_2 concentration of 10 mM, assuming that the CO_2 concentration profile is approximately linear within the catholyte, bubbling occurs when the CEL|cBL interface reaches saturation, and that there is near unity faradaic efficiency

for CO_2 regeneration, the boundary-layer thickness could be calculated as follows from Fick's Law.

$$L_{BL} = \frac{D_{CO_2,w} \times F(34\ [\mathrm{mM}] - 10[\mathrm{mM}])}{(20\ [\mathrm{mA\ cm^{-2}}])} \tag{S37}$$

The above expression results in a boundary layer of approximately 25 μm in thickness to match the CO_2 bubble onset seen experimentally.

S1.7 Diffusive and Ohmic Voltage Losses through AEL and CEL

The voltage losses due to diffusive and ohmic losses through the AEL and CEL are calculated using power loss analysis.[14,15]

$$V_{CEL} = \frac{\int_{CEL} \frac{-\boldsymbol{i}^2}{\kappa} - \boldsymbol{i} \cdot \frac{F}{\kappa} \sum_i z_i D_{i,CEL} \nabla c_i dx}{i_{tot}} \tag{S38}$$

$$V_{AEL} = \frac{\int_{AEL} \frac{-\boldsymbol{i}^2}{\kappa} - \boldsymbol{i} \cdot \frac{F}{\kappa} \sum_i z_i D_{i,CEL} \nabla c_i dx}{i_{tot}} \tag{S39}$$

where $\boldsymbol{i}$ is the local current density vector, i_{tot} is the total ionic current density in the BPM, and κ is the local ionic conductivity defined as follows:

$$\kappa = F^2 \sum_i \frac{z_i^2 D_i}{RT} c_i \tag{S40}$$

The first and second terms in Equations (S39) and (S40) represent the ohmic and diffusive losses, respectively, through the ion-exchange layers. Notably, evaluating the summed integral within Equations (S39) and (S40) is equivalent to calculating the electrostatic potential drop across a given ion-exchange layer, meaning that potential losses in the bulk membranes are fully described by ohmic and diffusive losses.

S2. Table of Parameters Employed in Model

Table S1: List of parameters employed in model.

SPECIES	DIFFUSIVITY	UNITS	REFERENCE
D_{K^+}	1.96×10^{-9}	$m^2\ s^{-1}$	16
D_{Na^+}	1.33×10^{-9}	$m^2\ s^{-1}$	16
D_{Cl^-}	2.03×10^{-9}	$m^2\ s^{-1}$	6
D_{H^+}	6.9645×10^{-9}	$m^2\ s^{-1}$	4
D_{OH^-}	4.96×10^{-9}	$m^2\ s^{-1}$	4
$D_{HCO_3^-}$	1.18×10^{-9}	$m^2\ s^{-1}$	16
$D_{CO_3^{2-}}$	9.55×10^{-10}	$m^2\ s^{-1}$	16
D_{CO_2}	1.91×10^{-9}	$m^2\ s^{-1}$	17

Table S2: List of buffer reaction constants

REACTION	CONSTANT	UNITS	REFERENCE
K_1	1×10^{-14}		18
k_1	2.861	$M\ s^{-1}$	18
K_2	4.27×10^{-7}		18
k_2	0.0371	$M\ s^{-1}$	18
K_3	4.58×10^{-11}		18
k_3	59.44	$M\ s^{-1}$	18
K_4	4.27×10^{7}		18

k_4	2.23×10^3	M s^{-1}	18
K_5	4.58×10^3		18
k_5	6.0×10^9	M s^{-1}	18

Table S3: List of membrane properties employed in model.

SPECIES	PARAMETER	UNITS	REFERENCE
IEC_{CEM}	1.8	mmol g^{-1}	19
ρ_{CEM}	1	g mL^{-1}	19
L_{CEM}	80	µm	19
$\lambda_{CEL,f_{H^+}=0}$	6		19
$\lambda_{CEL,f_{H^+}=1}$	9		19
IEC_{AEM}	1.8	mmol g^{-1}	19
ρ_{AEM}	1	g mL^{-1}	19
L_{AEM}	80	µm	19
$\lambda_{AEL,f_{OH^-}=0}$	6		19
$\lambda_{AEL,f_{OH^-}=1}$	9		19
$\frac{\varepsilon_{H_2O,M}}{\varepsilon_0}$	53.5		20
$\frac{\varepsilon_M}{\varepsilon_0}$	3.5		20

Table S4: List of concentrations in simulated seawater.

SPECIES	PARAMETER	UNITS	REF	NOTES
c_{Na^+}	0.5	M	21	
c_{Cl^-}	0.5 without divalent cations 0.626 with divalent cations	M	21	When running simulations with Ca^+ and Mg^{2+}, this value was adjusted accordingly to maintain electroneutrality.
$c_{HCO_3^-}$	0.0021	M	21	
$c_{CO_3^{2-}}$	2.03×10^{-5}	M	21	
c_{CO_2}	2.25×10^{-5}	M	21	
$c_{Mg^{2+}}$	0.053	M	21	Only present in simulations for divalent contaminants.
$c_{Ca^{2+}}$	0.010	M	21	Only present in simulations for divalent contaminants.

Table S5: List of fit parameters employed in model.

SPECIES	PARAMETER	UNITS	NOTES
$L_{\mathbf{Junction}}$	3.5	nm	Matches $L_{\mathbf{Junction}}$ value from Ref. 27.[19]
q	1	A. U.	Matches q value from Ref. 27.[19]
α_{WD}	0.33	A. U.	
$\varepsilon_{l,CL}$	0.253	A. U.	Catalyst layer pore volume. fraction

S3. Schematic of Experimental Cell for BPM Measurement

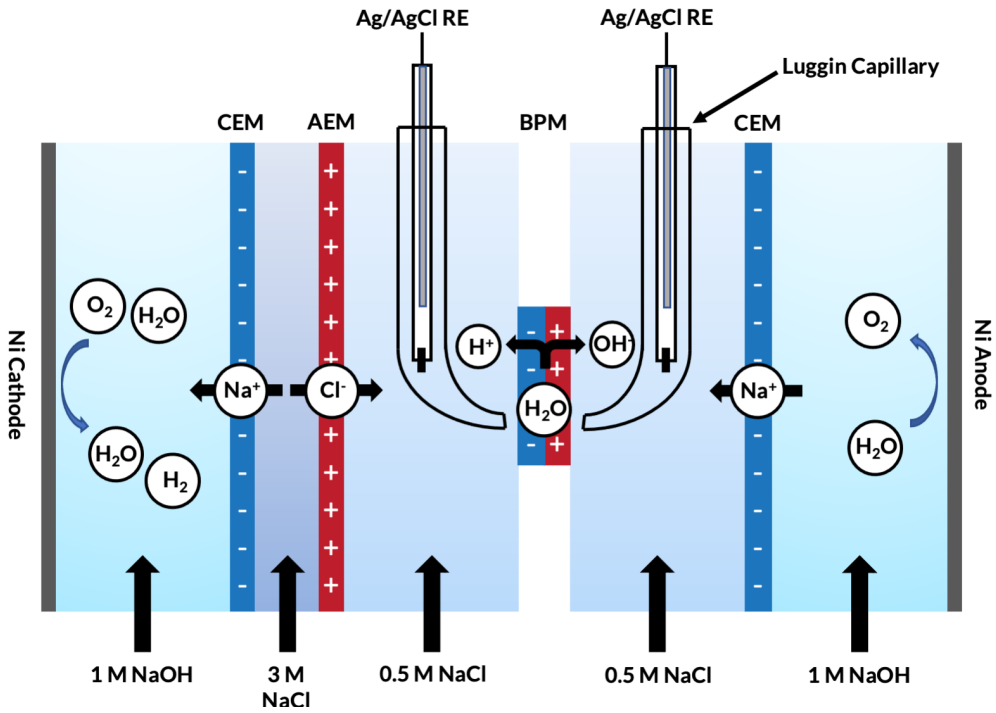

Figure S1: Cross sectional schematic of the five-chamber electrodialysis cell employed for experimental testing.

S4. CO_2 Efflux With and Without Phase Transfer

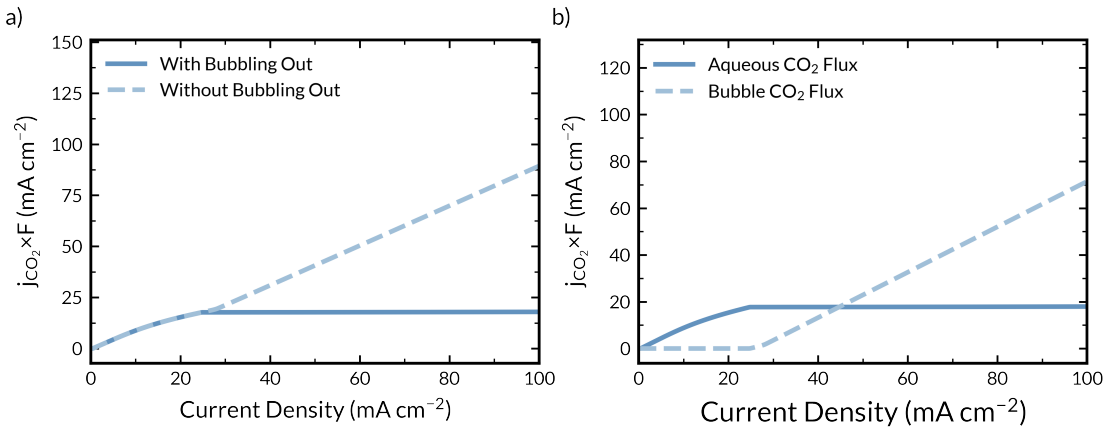

Figure S2: (a) Effect of CO_2 bubbling on the catholyte CO_2 flux for a BPM immersed in 1 M $KHCO_3$ as a function of applied current density. **(b)** Deconvoluted aqueous and bubble CO_2 fluxes for a BPM immersed in 1 M $KHCO_3$ as a function of applied current density.

S5. Comparison of Experiment and Simulation, $i < 20$ mA cm^{-2}

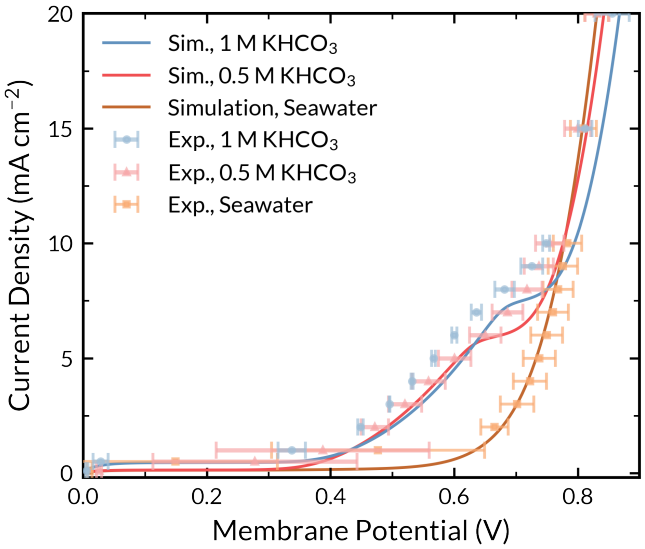

Figure S3: Comparison of experimental (markers) and simulated (solid lines) polarization curves from the 4-probe BPM measurement in various electrolytes for $i < 20$ mA cm^{-2} (within the salt crossover and bicarbonate dissociation regime).

S6: Understanding the Curve Shape of BPM Polarization Curves in Carbon-Containing Electrolytes

To resolve the origin of the early onset of electric-field-enhanced water dissociation, as well as to understand why the seawater BPM achieves higher current density for water dissociation at later voltages, the rates of dissociation reactions in the CL were replotted as a function of the maximum value of the electric field in the CL (**Figures S4-S7**). We choose to replot these dissociation rates as a function of maximum electric field, because the electric field is the driving force for the dissociation reactions in the CL. Additionally, we deconvolute the net dissociation rates into their contribution from the forward (dissociation) and reverse (recombination) pathways to evaluate which direction of the equilibrium reaction is affected by the change in electrolyte composition. First, we note that the seawater BPM possesses a larger maximum electric field than the 1 M $KHCO_3$ BPM at all applied potentials (**Figure S4**), and this relative increase in the interfacial electric field for the seawater BPM explains its greater current density observed at larger potentials where electric-field-enhanced water dissociation is dominant.

Next, we note that when the rate for the forward direction of water dissociation ($r_f = k_1(E)a_w$) is plotted against the electric field, it is unaffected by the choice of electrolyte (**Figure S5a**). This is intuitive, since we are plotting against the electric field, and these systems both possess a water activity of unity in the simulation, so all things equal, there should be no change in the forward rate of water dissociation. Conversely,

the simulation reveals that the presence of $KHCO_3$ noticeably reduces the rate of the reverse, recombination, reaction ($r_r = k_{-1}(E)a_{H^+}a_{OH^-}$)) compared to the seawater case (**Figure S5b**).

Further analysis of the average concentration of (bi)carbonate species, protons, and hydroxide anions within the BPM CL (**Figure S11-S12**) elucidates how the 1 M $KHCO_3$ electrolyte suppresses H^+-OH^- recombination at low potentials. The simulations reveal that HCO_3^- anion species react readily with OH^- within the BPM CL to form CO_3^{2-} through homogeneous reaction (**Figure S10**), scavenging OH^- formed in the forward, dissociation reactions, and reducing the relative rate of H^+-OH^- recombination. Consequently, the reduction in H^+-OH^- recombination rate incurred upon application of the $KHCO_3$ electrolyte manifests in a seemingly accelerated onset of the net water dissociation reaction in a 1 M $KHCO_3$ electrolyte**.** Importantly, when the HCO_3^- anions in the junction are fully depleted (at ~0.75 V), the rate of recombination for the seawater and 1 M $KHCO_3$ BPMs become equal for a given electric field driving force (**Figure S5, S8**).

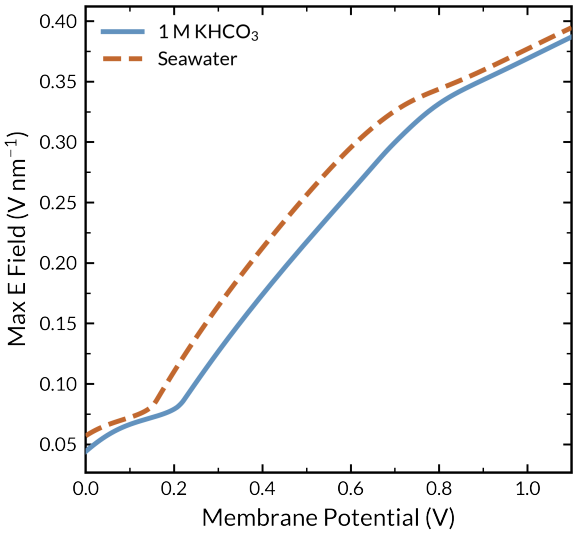

Figure S4: Simulated maximum electric field in the CL as a function of applied membrane potential for a BPM immersed in 1 M $KHCO_3$ (solid blue line) and simulated seawater (orange dashed lines).

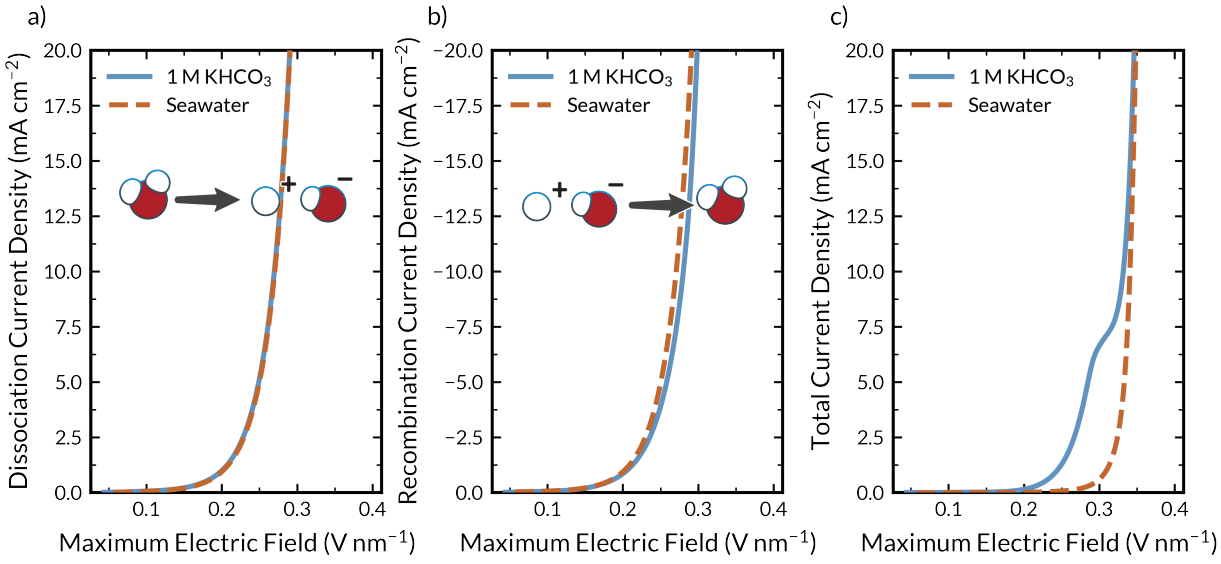

Figure S5: Calculated current generated by water dissociation as a function of maximum electric field in the CL for a BPM immersed in 1 M $KHCO_3$ (blue solid lines) and seawater (orange dashed lines). **(a)** Dissociation rate integrated within catalyst layer ($F\int_{L_{CL}} k_1(E)a_w dx$). **(b)** Recombination rate ($F\int_{L_{CL}} k_{-1}(E)a_{H^+}a_{OH^-}dx$). **(c)** Total rate ($F\int_{L_{CL}} R_1 dx$).

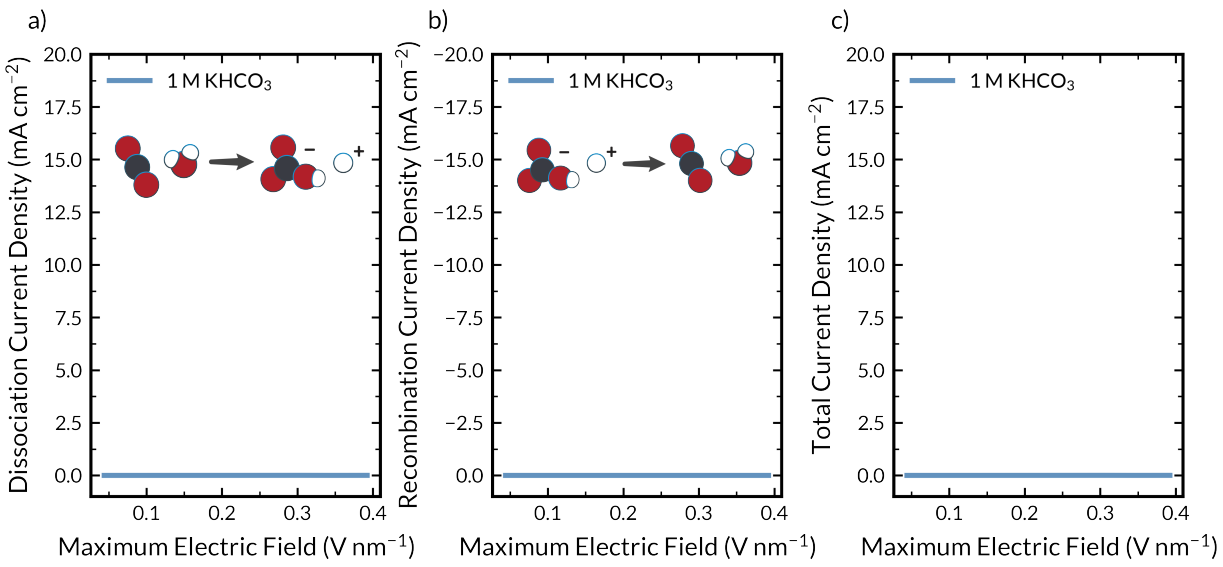

Figure S6: Calculated current generated by CO_2 dissociation as a function of maximum electric field in the CL for a BPM immersed in 1 M $KHCO_3$ (blue solid lines) and seawater (orange dashed lines). **(a)** Dissociation rate integrated within catalyst layer ($F\int_{L_{CL}} k_2(E)a_w a_{CO_2} dx$). **(b)** Recombination rate ($F\int_{L_{CL}} k_{-2}(E)a_{H^+}a_{HCO_3^-} dx$). **(c)** Total rate ($F\int_{L_{CL}} R_2 dx$).

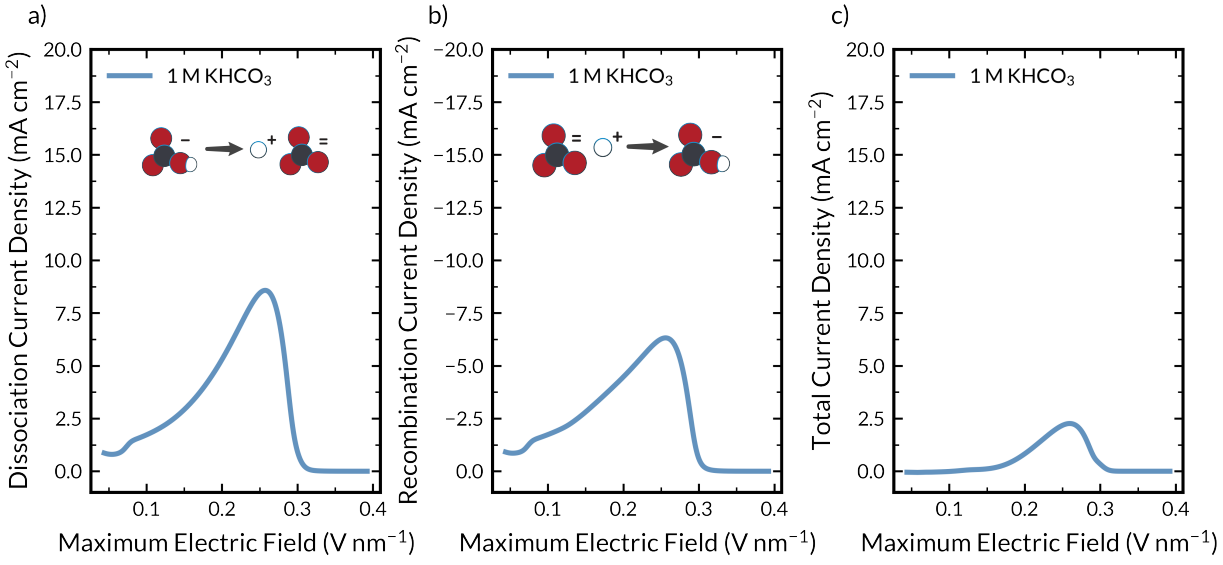

Figure S7: Calculated current generated by bicarbonate dissociation as a function of maximum electric field in the CL for a BPM immersed in 1 M $KHCO_3$ (blue solid lines) and seawater (orange dashed lines). **(a)** Dissociation rate integrated within catalyst layer ($F\int_{L_{CL}} k_3(E)a_{HCO_3^-} dx$). **(b)** Recombination rate ($F\int_{L_{CL}} k_{-3}(E)a_{H^+}a_{CO_3^{2-}} dx$). **(c)** Total rate $F\int_{L_{CL}} R_3 dx$).

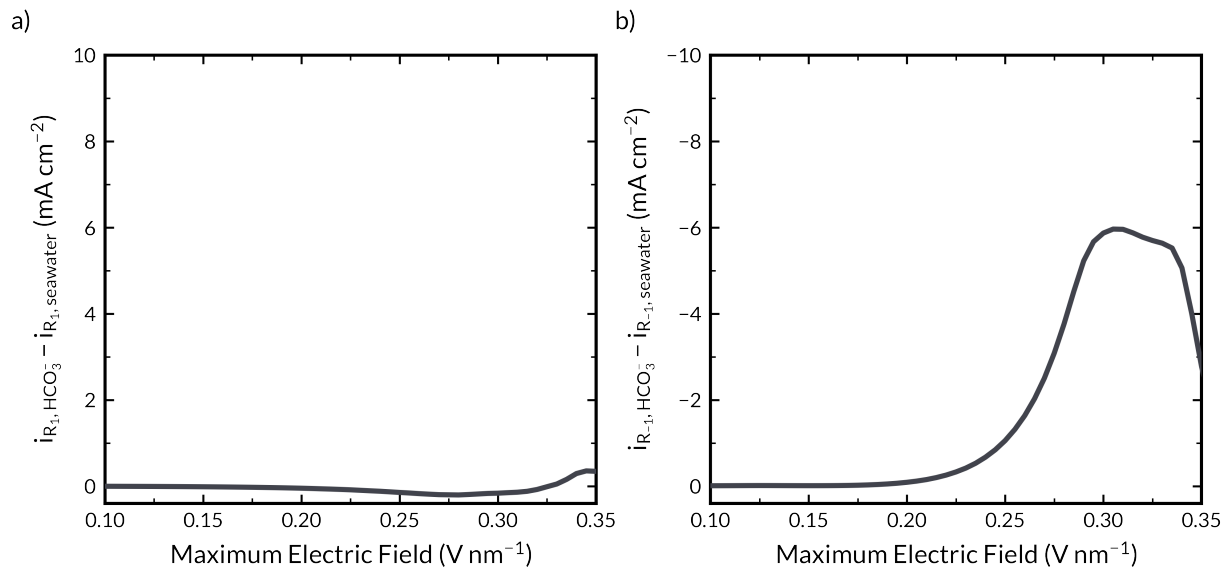

Figure S8: Difference in water **(a)** dissociation and **(a)** recombination current density between a BPM immersed in 1 M $KHCO_3$ and simulated seawater as a function of maximum electric field within the catalyst layer.

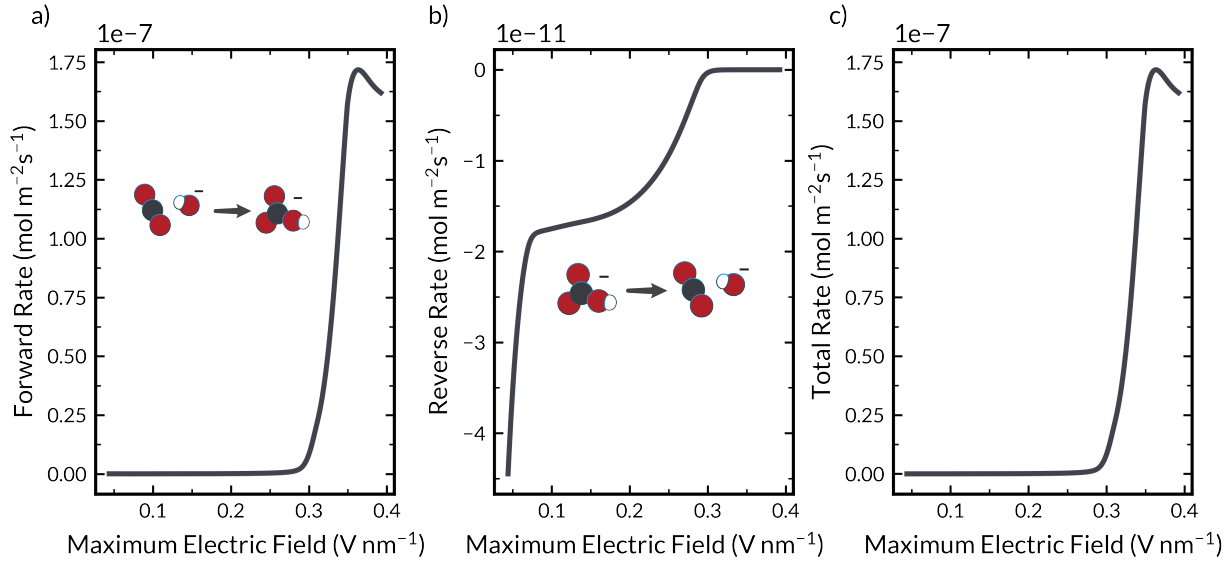

Figure S9: Calculated species interconversion between CO_2 and HCO_3^- as a function of maximum electric field in the CL for a BPM immersed in 1 M $KHCO_3$ (blue solid lines) and seawater (orange dashed lines). **(a)** Forward rate integrated within catalyst layer ($\int_{L_{CL}} k_4(E) a_{CO_2} a_{OH^-} dx$). **(b)** Recombination rate ($\int_{L_{CL}} k_{-4}(E) a_{HCO_3^-} dx$). **(c)** Total rate $\int_{L_{CL}} R_4 dx$).

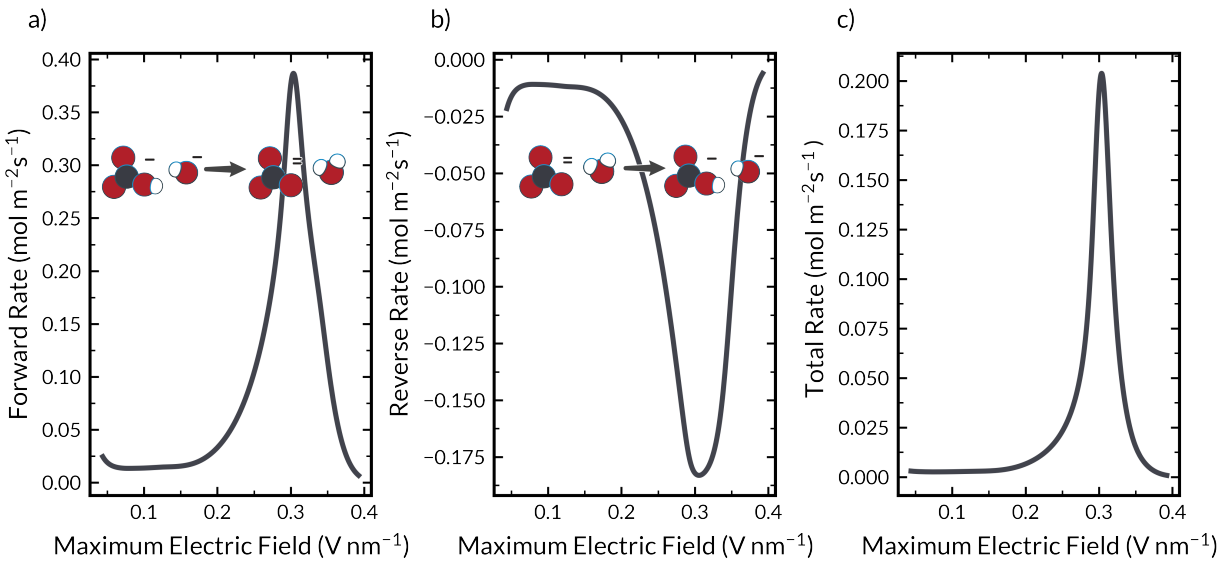

Figure S10: Calculated species interconversion between HCO_3^- and CO_3^{2-} as a function of maximum electric field in the CL for a BPM immersed in 1 M $KHCO_3$ (blue solid lines) and seawater (orange dashed lines). **(a)** Forward rate integrated within catalyst layer ($\int_{L_{CL}} k_5(E) a_{HCO_3^-} a_{OH^-} dx$). **(b)** Recombination rate ($\int_{L_{CL}} k_{-5}(E) a_{CO_3^{2-}} dx$). **(c)** Total rate $\int_{L_{CL}} R_5 dx$).

S7: Calculated Average Concentrations within the BPM CL

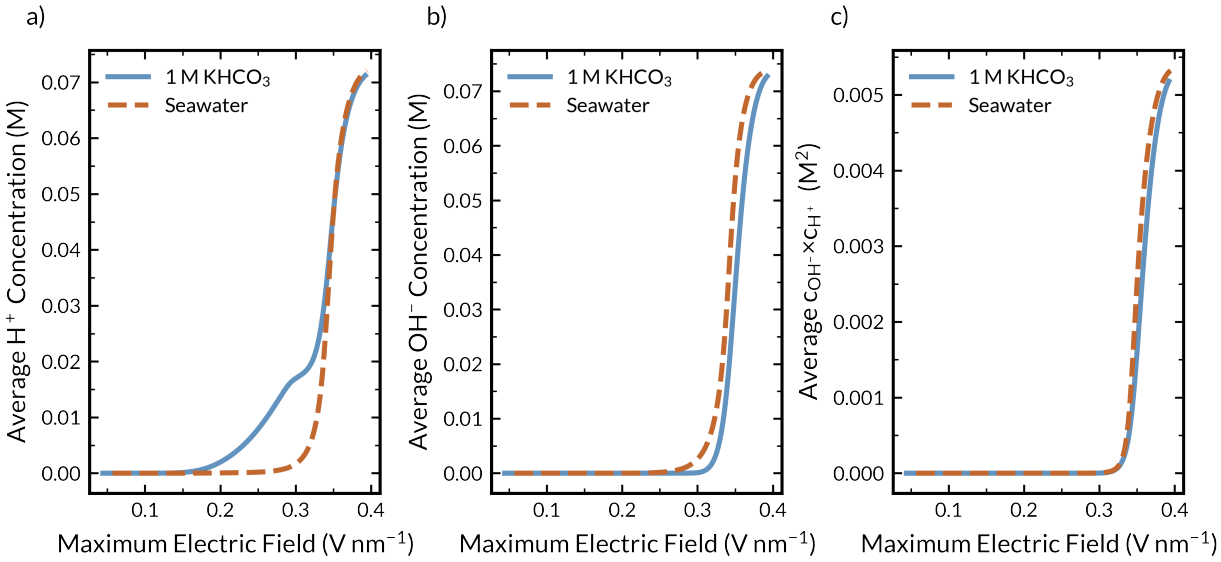

Figure S11: Calculated average **(a)** H^+, **(b)** OH^-, and **(c)** product of H^+ and OH^- concentrations within the BPM CL as a function of maximum electric field in the CL.

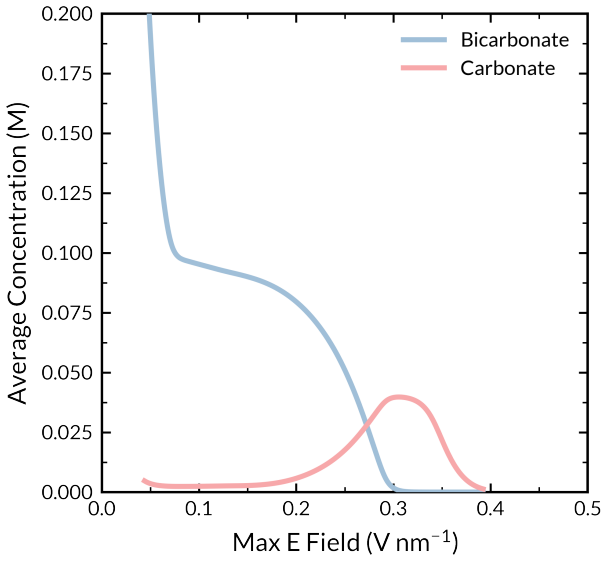

Figure S12: Calculated average bicarbonate (blue) and carbonate (red) concentration within the BPM catalyst layer for a BPM immersed in **(a)** 1 M $KHCO_3$ and **(b)** simulated seawater.

S8: Concentration Profiles for a BPM Immersed in 1 M $KHCO_3$

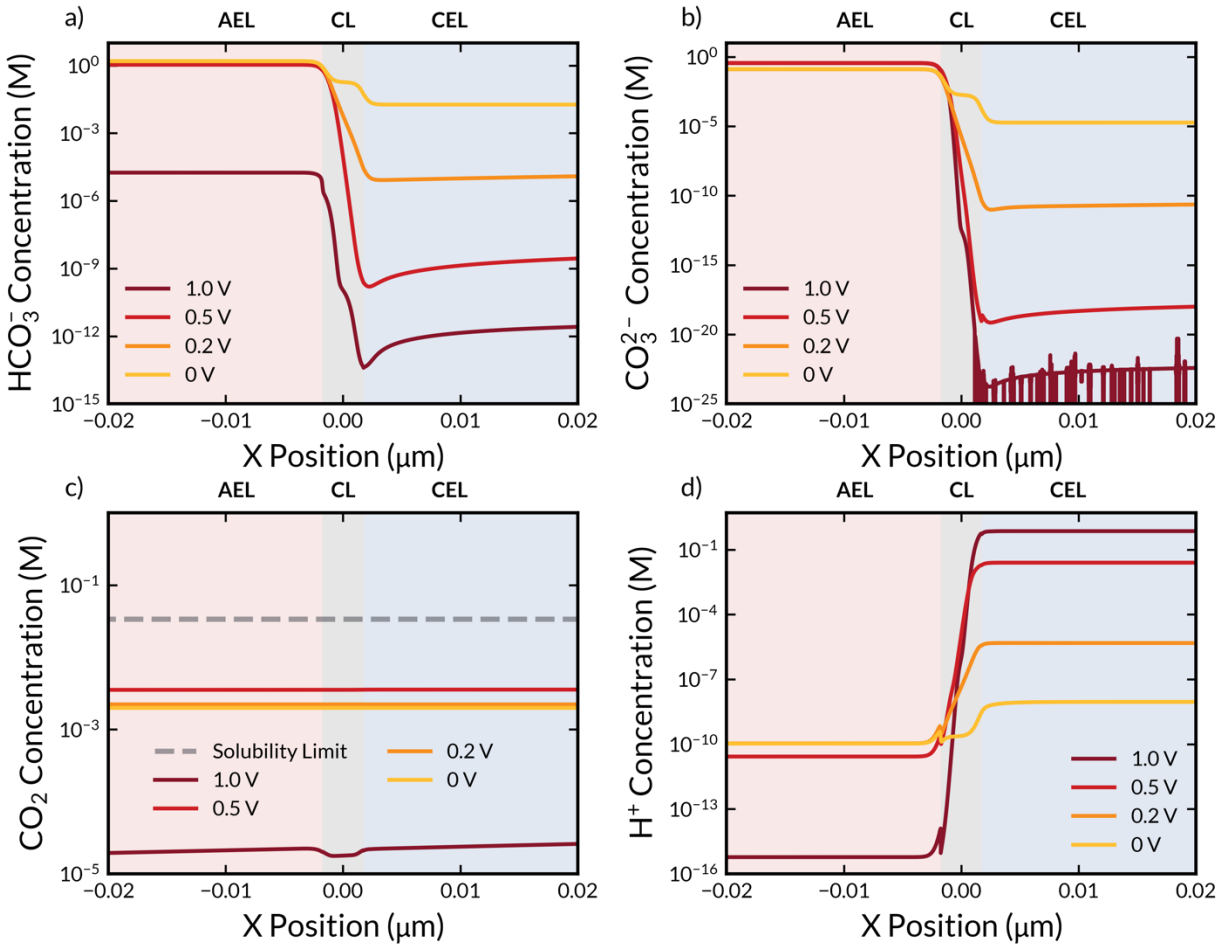

Figure S13: Simulated concentration profiles of **(a)** HCO_3^-, **(b)** CO_3^{2-}, **(c)** dissolved CO_2, and **(d)** H^+ within a BPM immersed in 1 M $KHCO_3$ at applied membrane voltages of 0 V, 0.2 V, 0.5 V, and 1.0 V. Zoomed into the AEL|CEL interface. Grey-dashed line in panel **(c)** denotes the solubility limit of CO_2 in water.

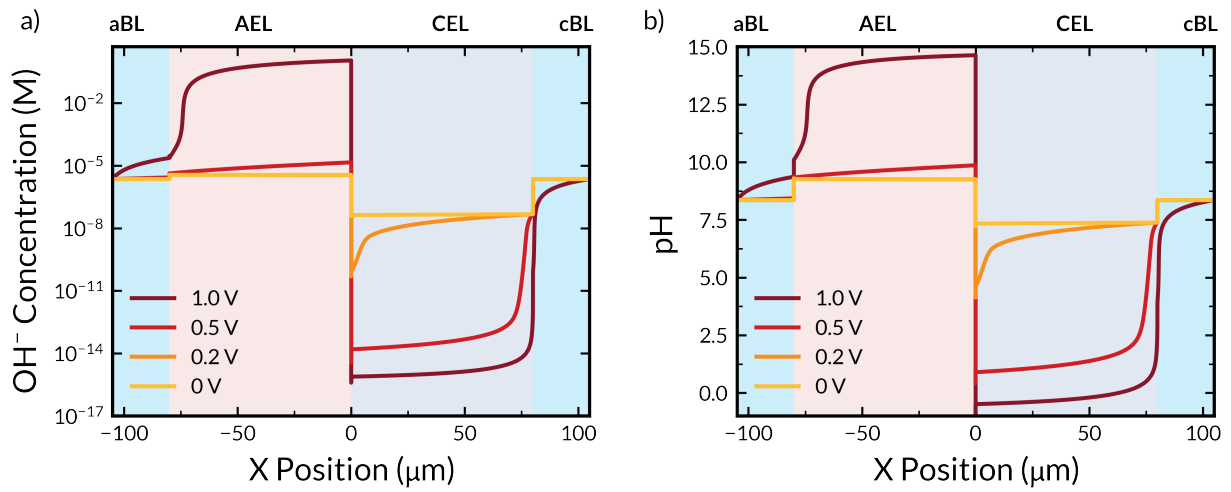

Figure S14: Simulated concentration profiles of **(a)** OH^-, and **(b)** pH within a BPM immersed in 1 M $KHCO_3$ at applied membrane voltages of 0 V, 0.2 V, 0.5 V, and 1.0 V.

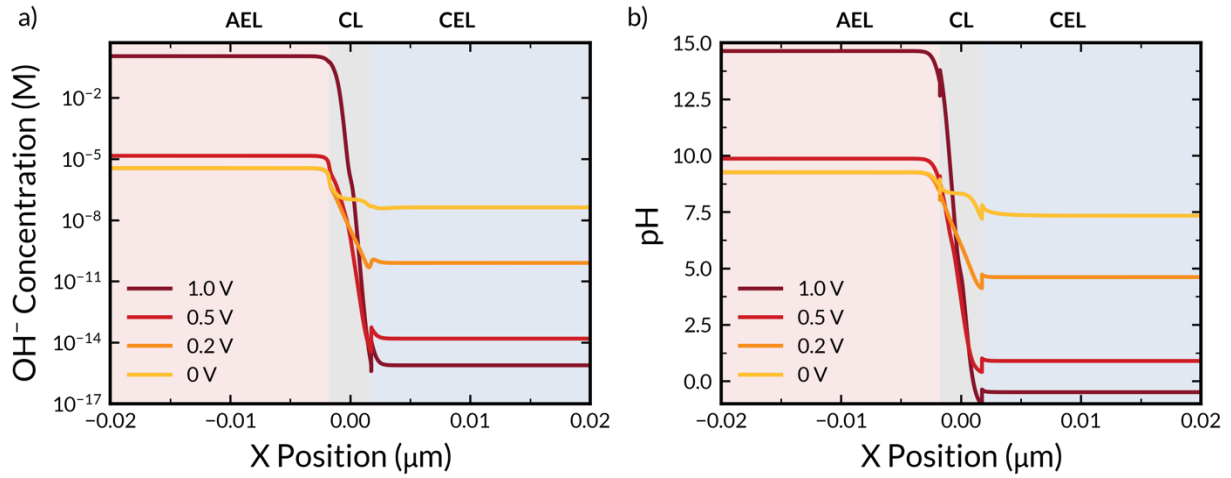

Figure S15: Simulated concentration profiles of **(a)** OH^-, and **(b)** pH within a BPM immersed in 1 M $KHCO_3$ at applied membrane voltages of 0 V, 0.2 V, 0.5 V, and 1.0 V. Zoomed into the AEL | CEL interface.

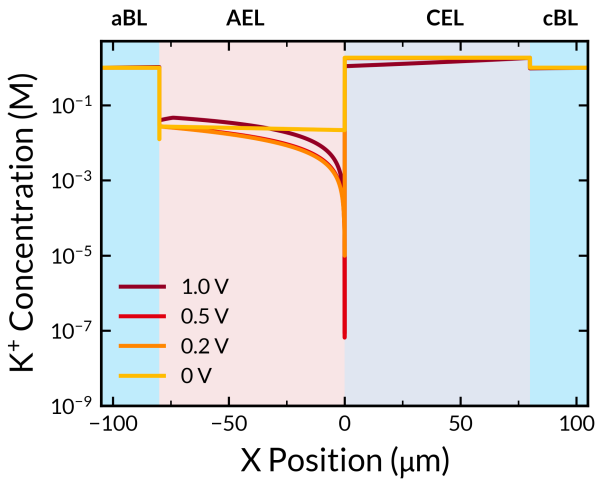

Figure S16: Simulated concentration profiles of K^+ within a BPM immersed in 1 M $KHCO_3$ at applied membrane voltages of 0 V, 0.2 V, 0.5 V, and 1.0 V.

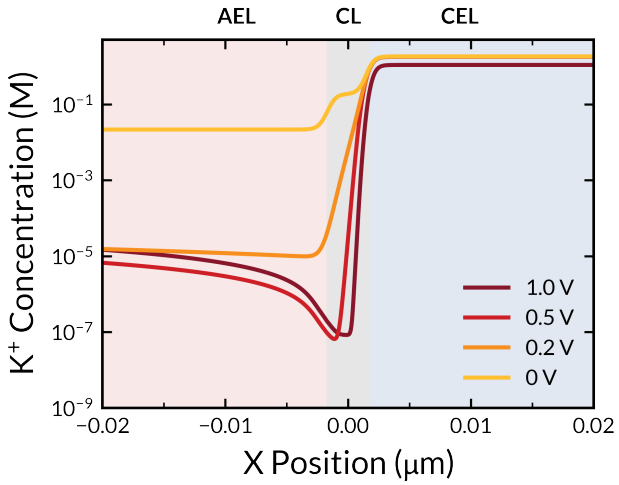

Figure S17: Simulated concentration profiles of K^+ within a BPM immersed in 1 M $KHCO_3$ at applied membrane voltages of 0 V, 0.2 V, 0.5 V, and 1.0 V. Zoomed into the AEL|CEL interface.

S9: Concentration Profiles for a BPM Immersed in Seawater

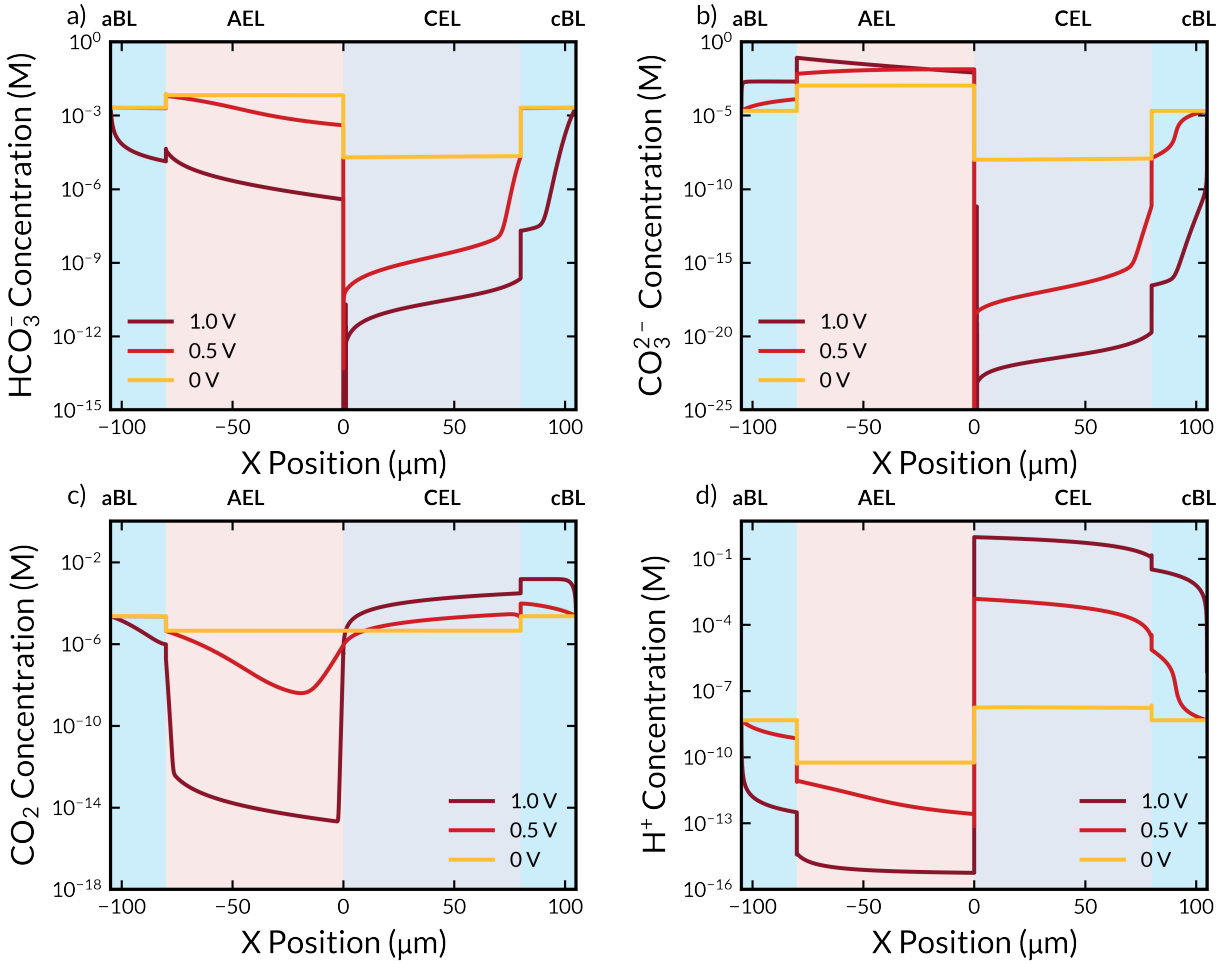

Figure S18: Simulated concentration profiles of **(a)** HCO_3^-, **(b)** CO_3^{2-}, **(c)** CO_2, and **(d)** H^+ within a BPM immersed in simulated seawater at applied membrane voltages of 0 V, 0.5 V, and 1.0 V.

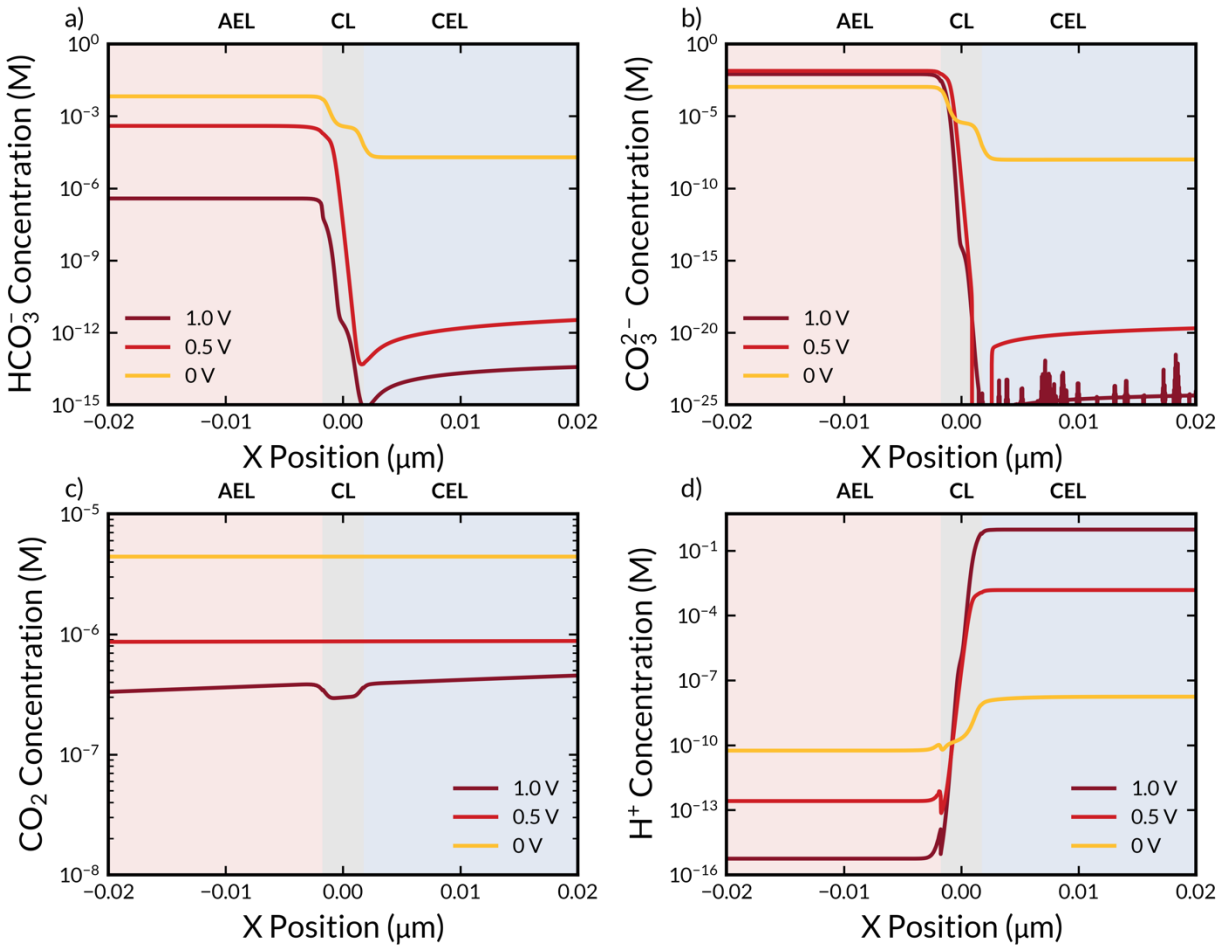

Figure S19: Simulated concentration profiles of **(a)** HCO_3^-, **(b)** CO_3^{2-}, **(c)** CO_2, and **(d)** H^+ within a BPM immersed in simulated seawater at applied membrane voltages of 0 V, 0.2 V, 0.5 V, and 1.0 V. Zoomed into AEL|CEL interface.

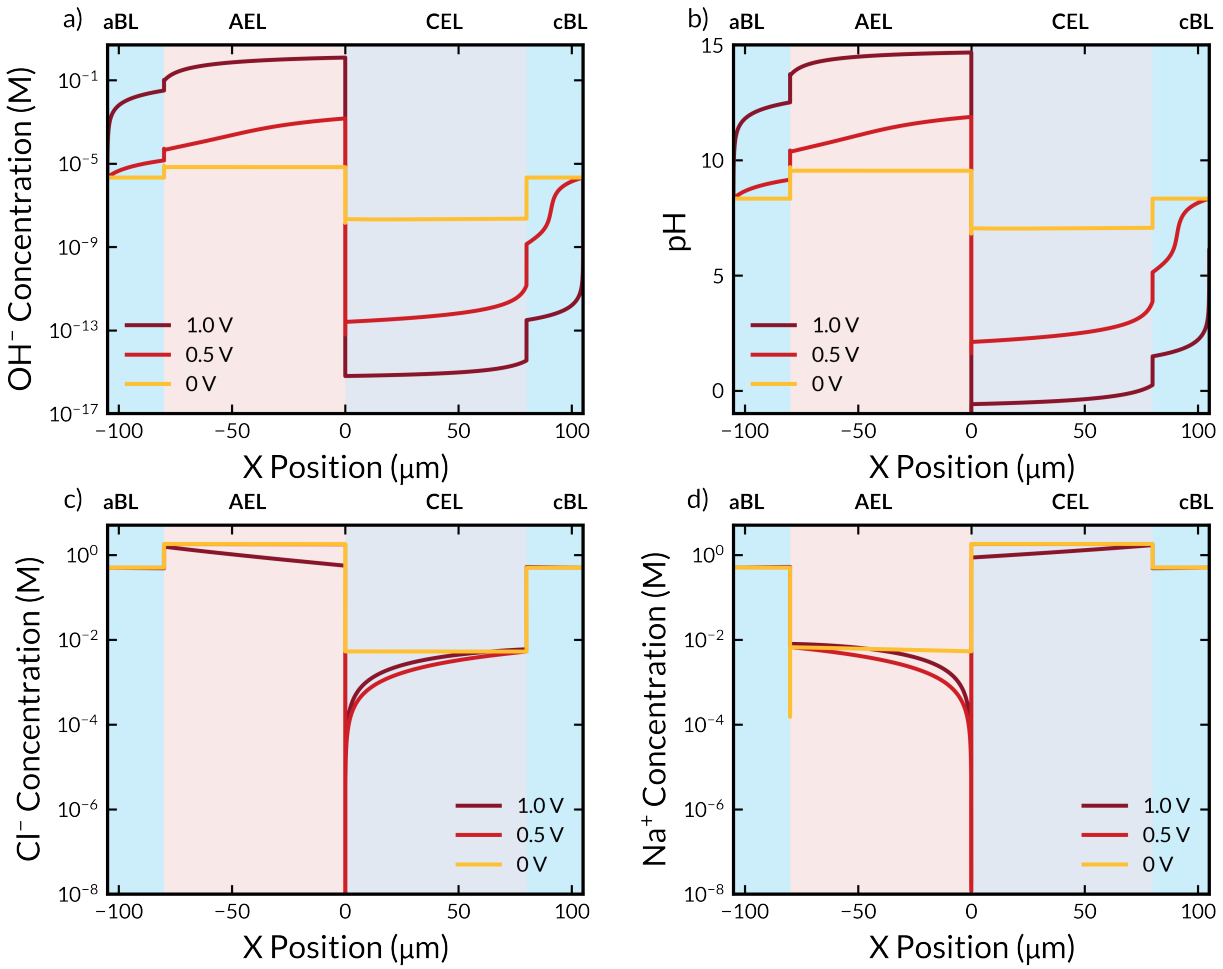

Figure S20: Simulated profiles of **(a)** OH^-, **(b)** pH, **(c)** Cl^-, and **(d)** Na^+ within a BPM immersed in simulated seawater at applied membrane voltages of 0 V, 0.5 V, and 1.0 V.

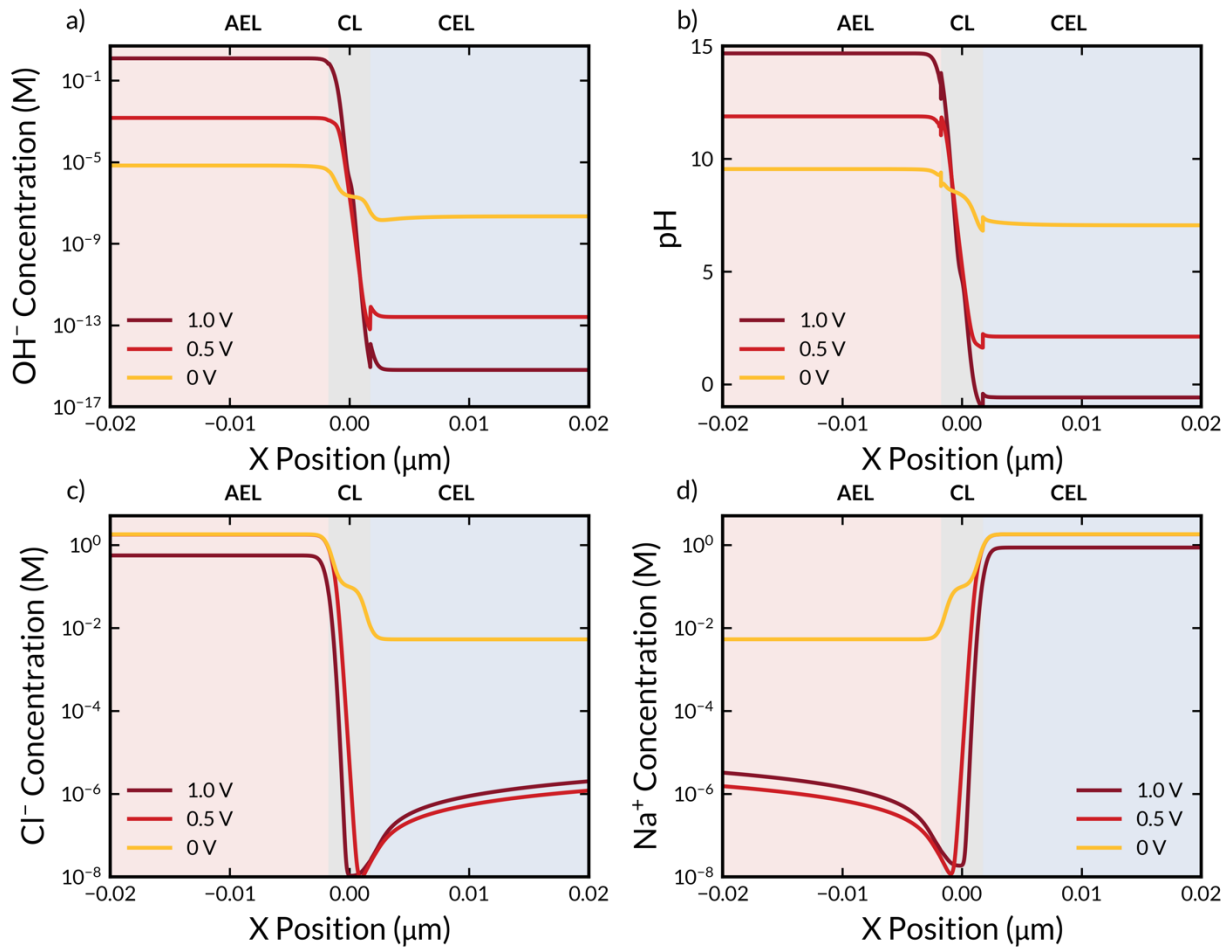

Figure S21: Simulated profiles of **(a)** OH^-, **(b)** pH, **(c)** Cl^-, and **(d)** Na^+ within a BPM immersed in simulated seawater at applied membrane voltages of 0 V, 0.5 V, and 1.0 V. Zoomed into AEL|CEL interface.

S10: Electrostatic Potential Profiles

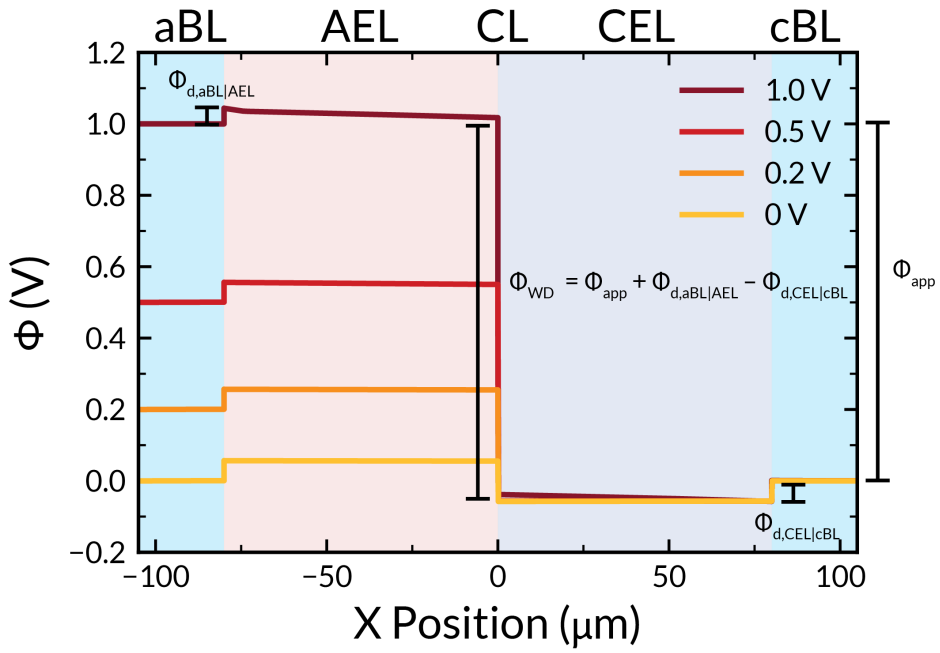

Figure S22: Simulated electrostatic potential profile of a BPM immersed in 1 M $KHCO_3$ operating at 0 V, 0.2 V, 0.5 V, and 1.0 V.

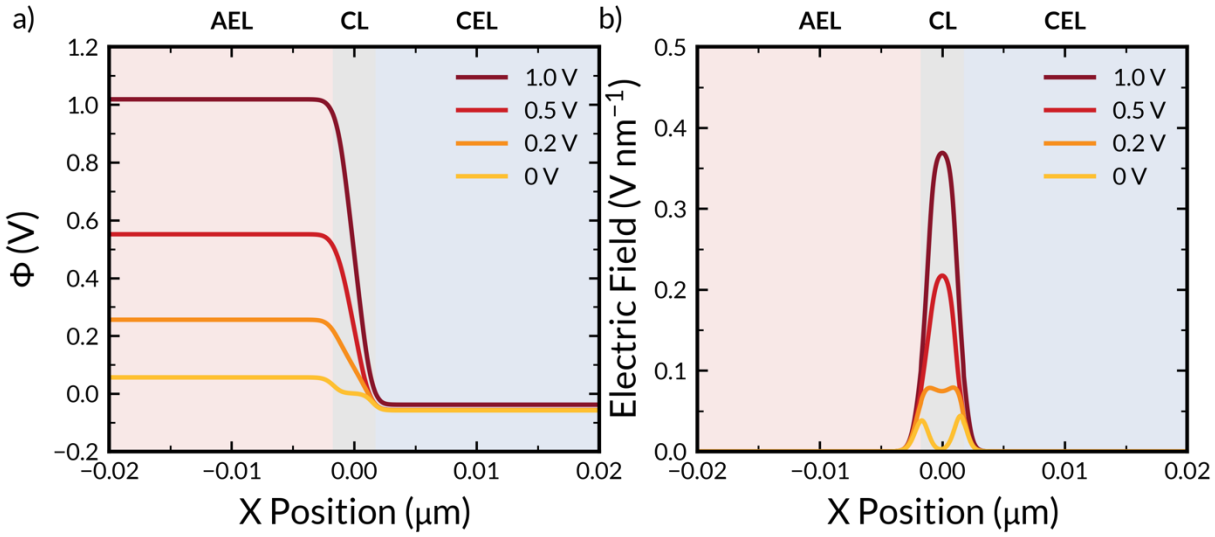

Figure S23: Simulated **(a)** electrostatic potential and **(b)** electric field profile of a BPM immersed in 1 M $KHCO_3$ operating at 0 V, 0.2 V, 0.5 V, and 1.0 V. Zoomed into AEL|CEL interface.

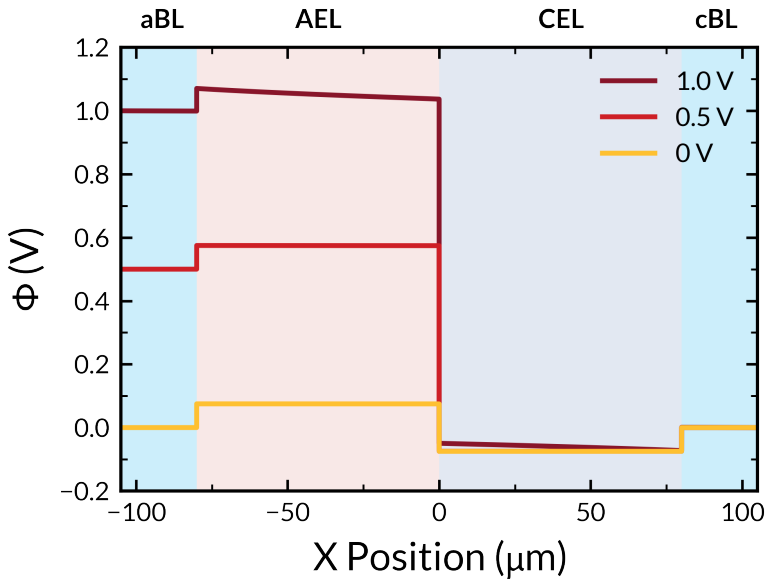

Figure S24: Simulated electrostatic potential profile of a BPM immersed in simulated seawater operating at 0 V, 0.5 V, and 1.0 V.

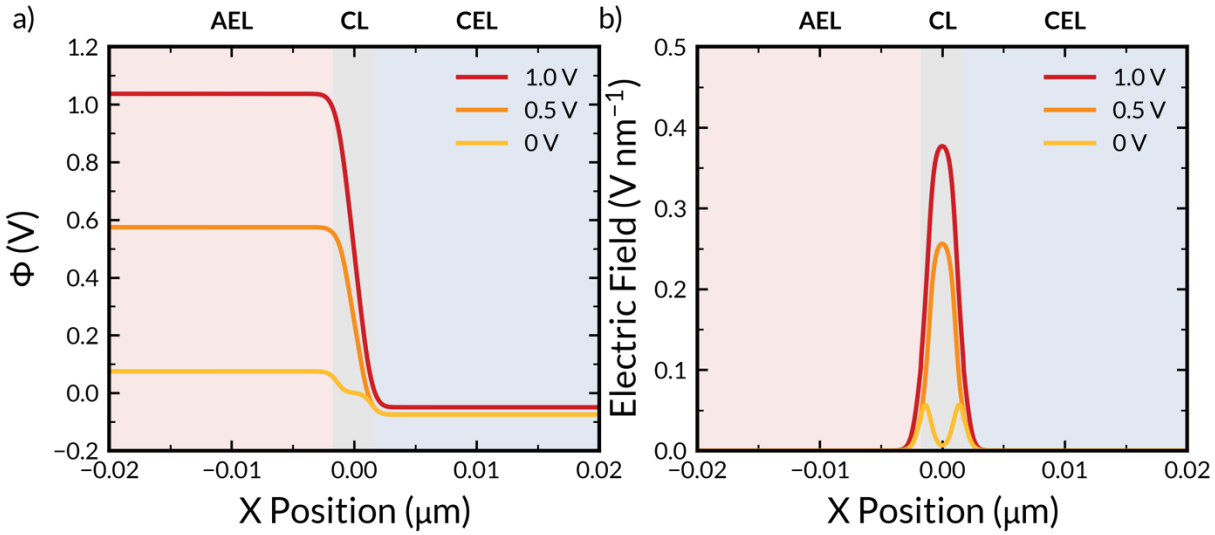

Figure S25: Simulated **(a)** electrostatic potential and **(b)** electric field profile of a BPM immersed in simulated seawater operating at 0 V, 0.5 V, and 1.0 V. Zoomed into AEL|CEL interface.

S11: Deviation of Homogeneous Reactions from Equilibrium

S11.1 Definition of Equilibrium Deviation

The equilibrium deviation of a given homogeneous buffer reaction is defined as follows:

$$K_i\ Deviation = \frac{k_i \prod_{s_{i,n}<0} a_i^{-s_{i,n}}}{k_{-i} \prod_{s_{i,n}>0} a_i^{s_{i,n}}} \tag{S41}$$

If the forward and backward rates are equal, (their ratio is 1), the reactions are in equilibrium. If the ratio is greater than 1, the forward rate is favored, and if the ratio is less than 1, the reverse rate is favored.

S11.2 Simulated Equilibrium Deviation

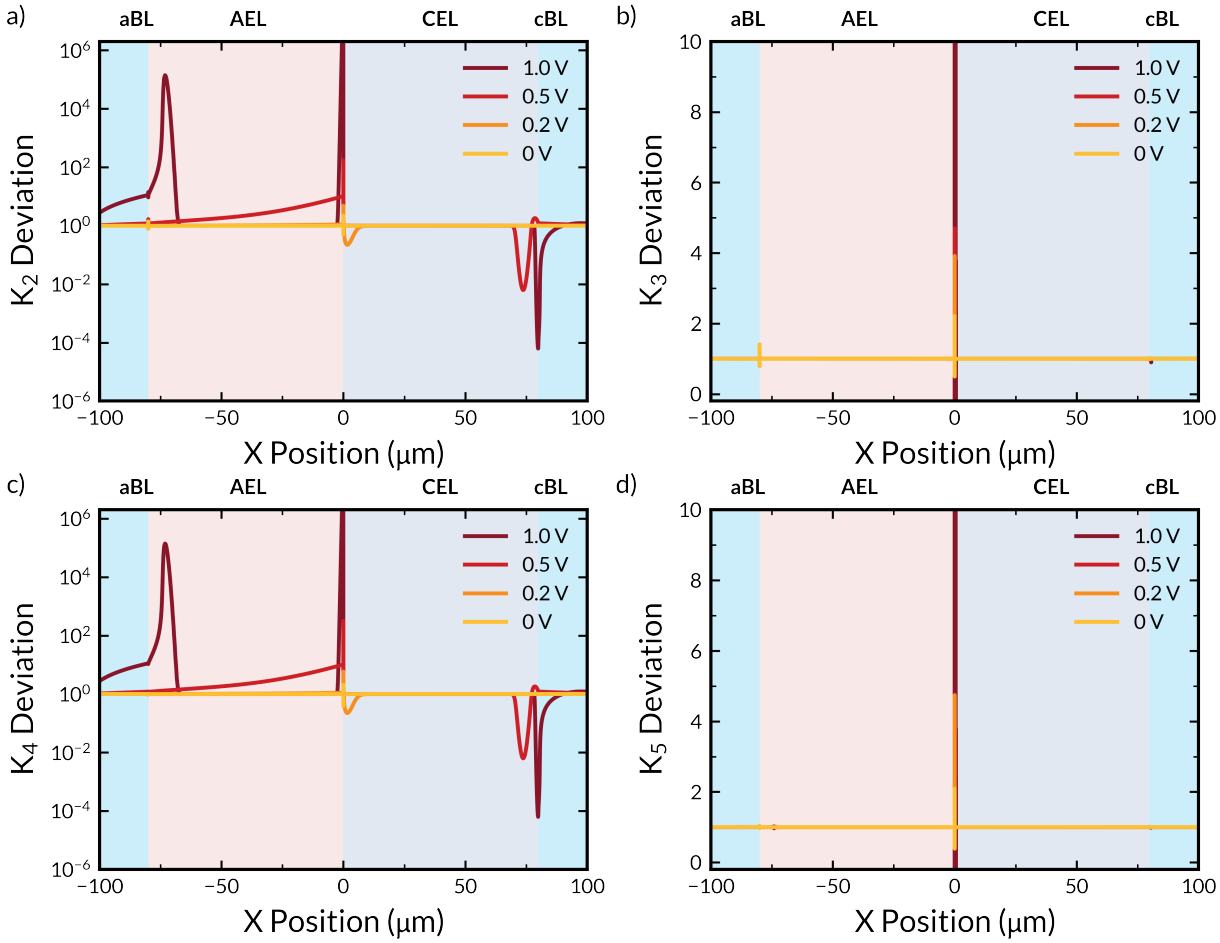

Figure S26: (a-d) Simulated deviation of homogeneous reactions (2-5) from equilibrium within a BPM immersed in 1 M $KHCO_3$.

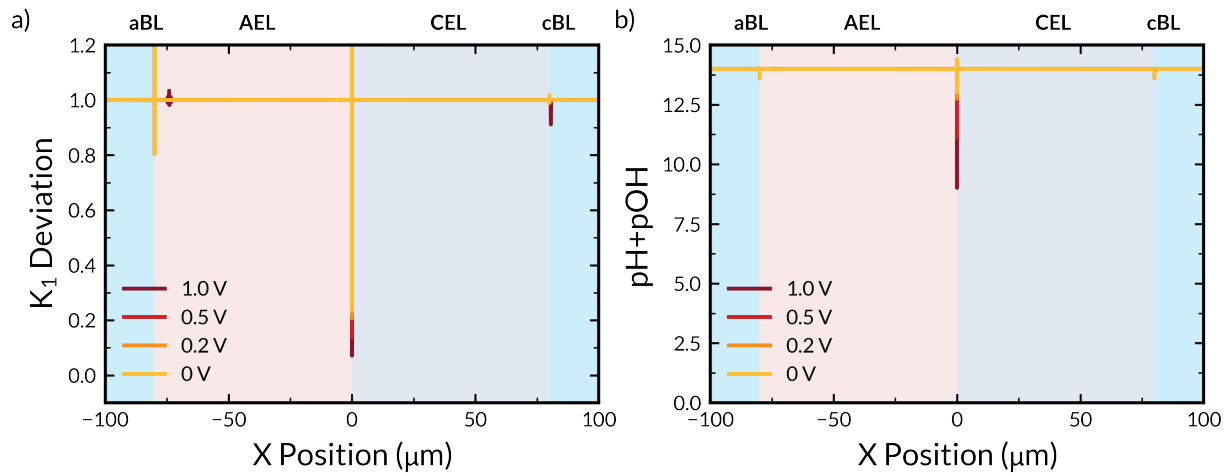

Figure S27: (a) Simulated deviation of homogeneous reaction (1) from equilibrium within a BPM immersed in 1 M $KHCO_3$. **(b)** Simulated pH + pOH within a BPM immersed in 1 M $KHCO_3$.

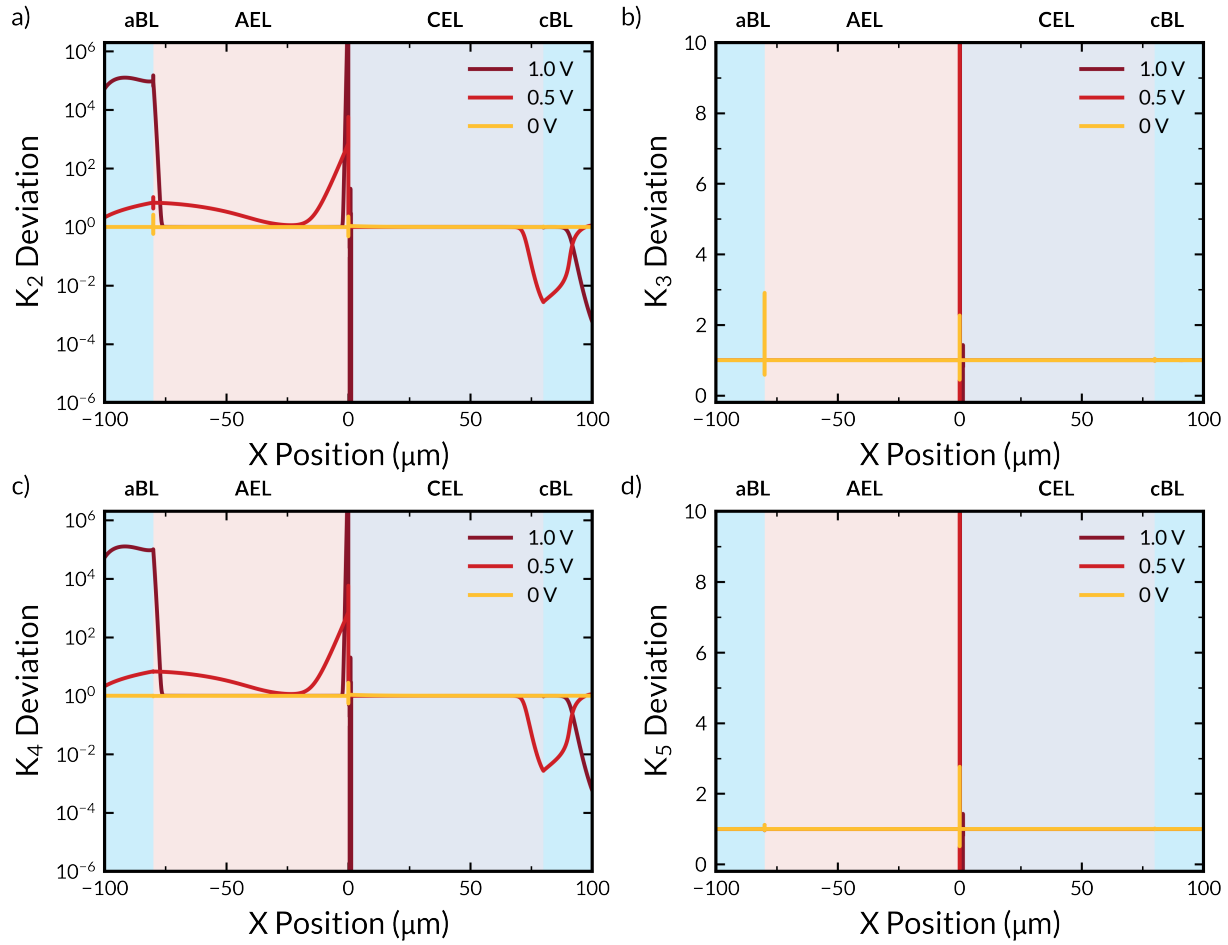

Figure S28: (a-d) Simulated deviation of homogeneous reactions (2-4) from equilibrium within a BPM immersed in simulated seawater.

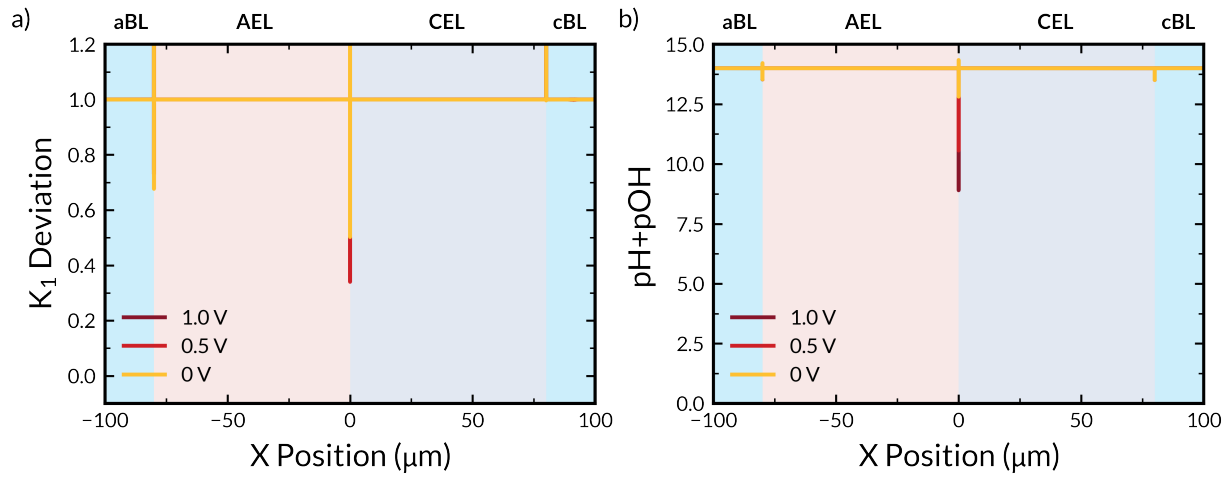

Figure S29: **(a)** Simulated deviation of homogeneous reaction (1) from equilibrium within a BPM immersed in simulated seawater. **(b)** Simulated pH + pOH within a BPM immersed in simulated seawater.

S12. Breakdown of BPM Current Density in a BPM in 1 M $KHCO_3$, $i < 20$ mA cm^{-2}

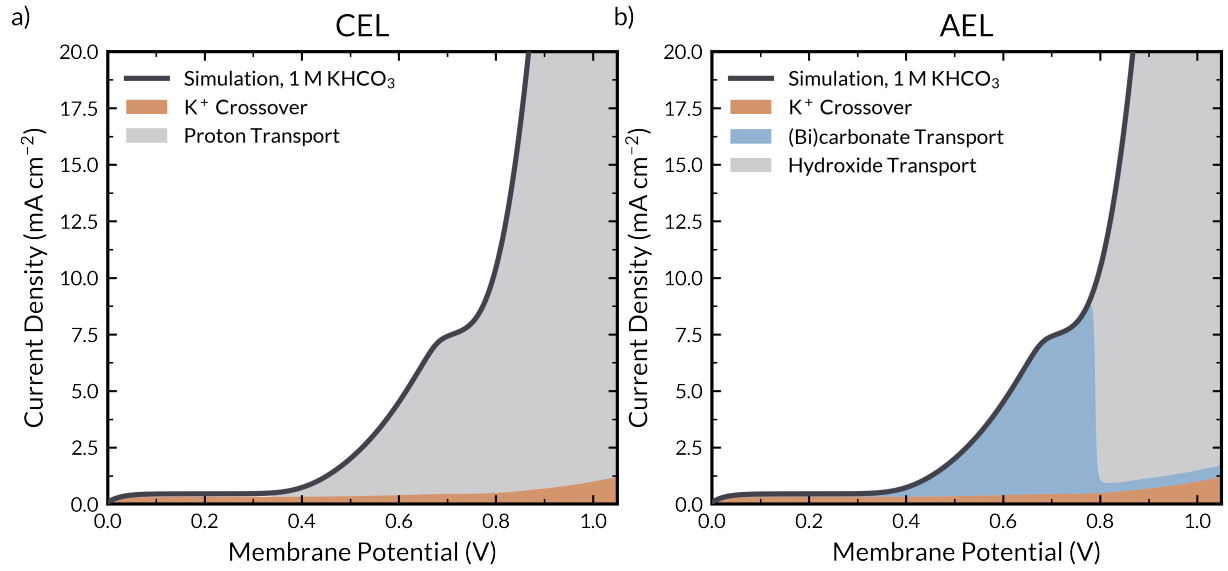

Figure S30: Breakdown of BPM current density in the CEL and AEL of a BPM immersed in 1 M $KHCO_3$ for i < 20 mA cm^{-2}. Orange area represents current density carried by K^+. Blue area represents current carried by (bi)carbonates. Grey area represents current density carried by protons or hydroxides in the CEL or AEL, respectively.

S13: Effective Transference Number Profiles for a BPM Immersed in 1 M $KHCO_3$

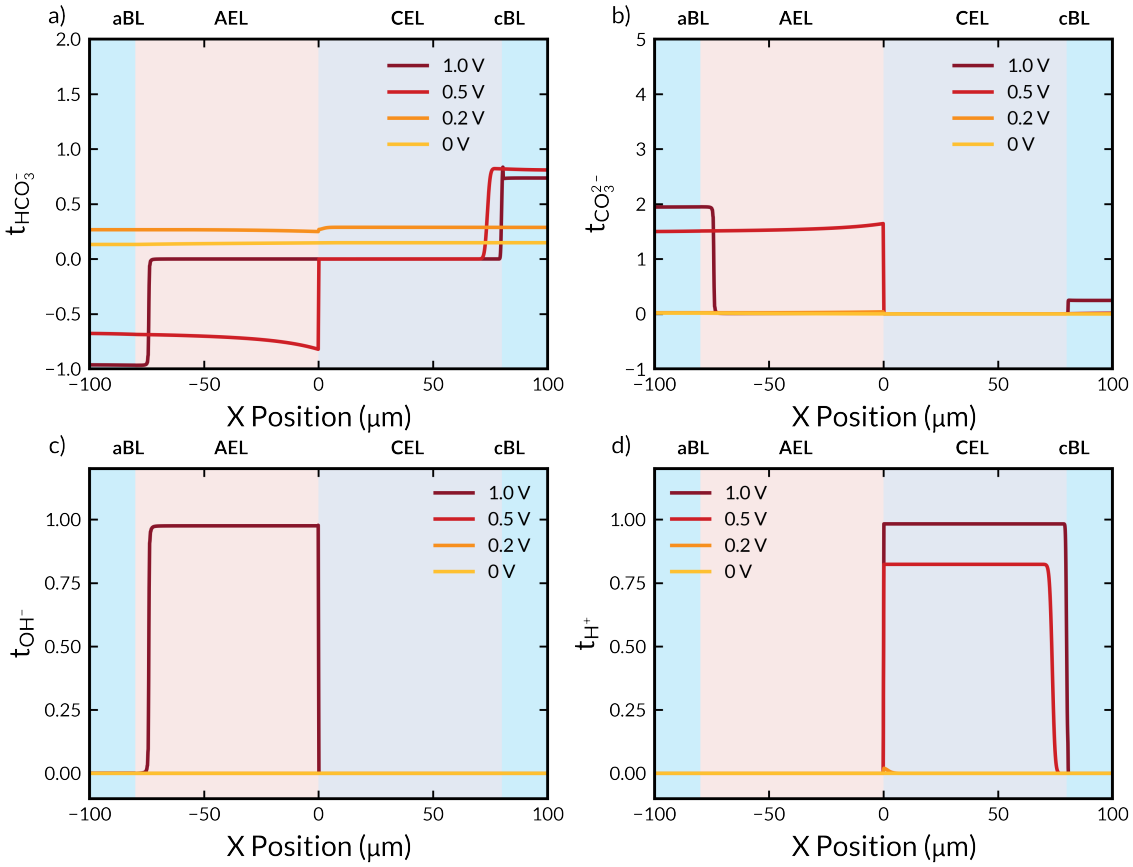

Figure S31: Simulated effective transference profiles of **(a)** HCO_3^-, **(b)** CO_3^{2-}, **(c)** OH^-, and **(d)** H^+ within a BPM immersed in 1 M $KHCO_3$ at applied membrane voltages of 0 V, 0.2 V, 0.5 V, and 1.0 V.

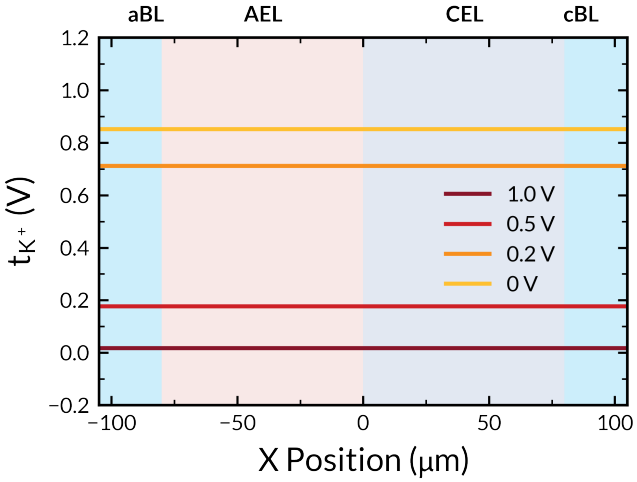

Figure S32: Simulated effective transference number profiles of K^+ within a BPM immersed in 1 M $KHCO_3$ at applied membrane voltages of 0 V, 0.2 V, 0.5 V, and 1.0 V.

S14: Effective Transference Number Profiles for a BPM Immersed in Seawater

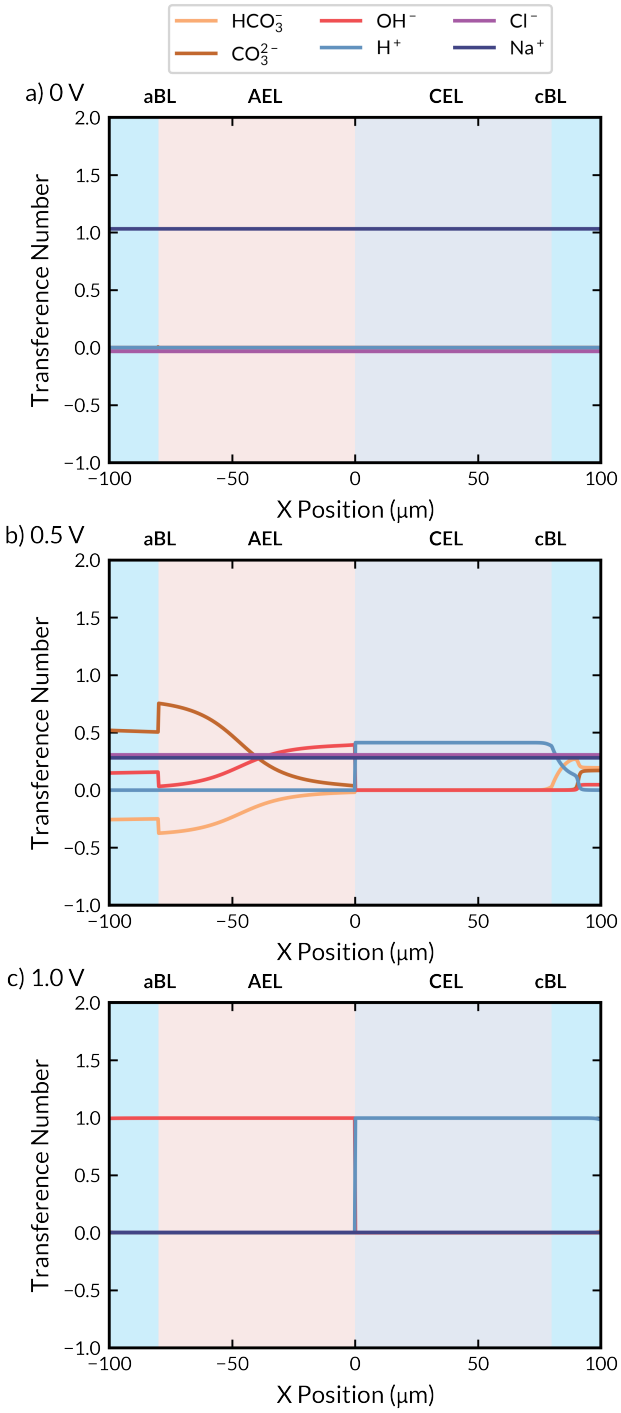

Figure S33: Simulated effective transference number profiles of HCO_3^-, CO_3^{2-}, H^+, OH^-, and K^+ within a BPM immersed in simulated seawater at applied membrane voltages of **(a)** 0 V, **(b)** 0.5 V, and **(c)** 1.0 V.

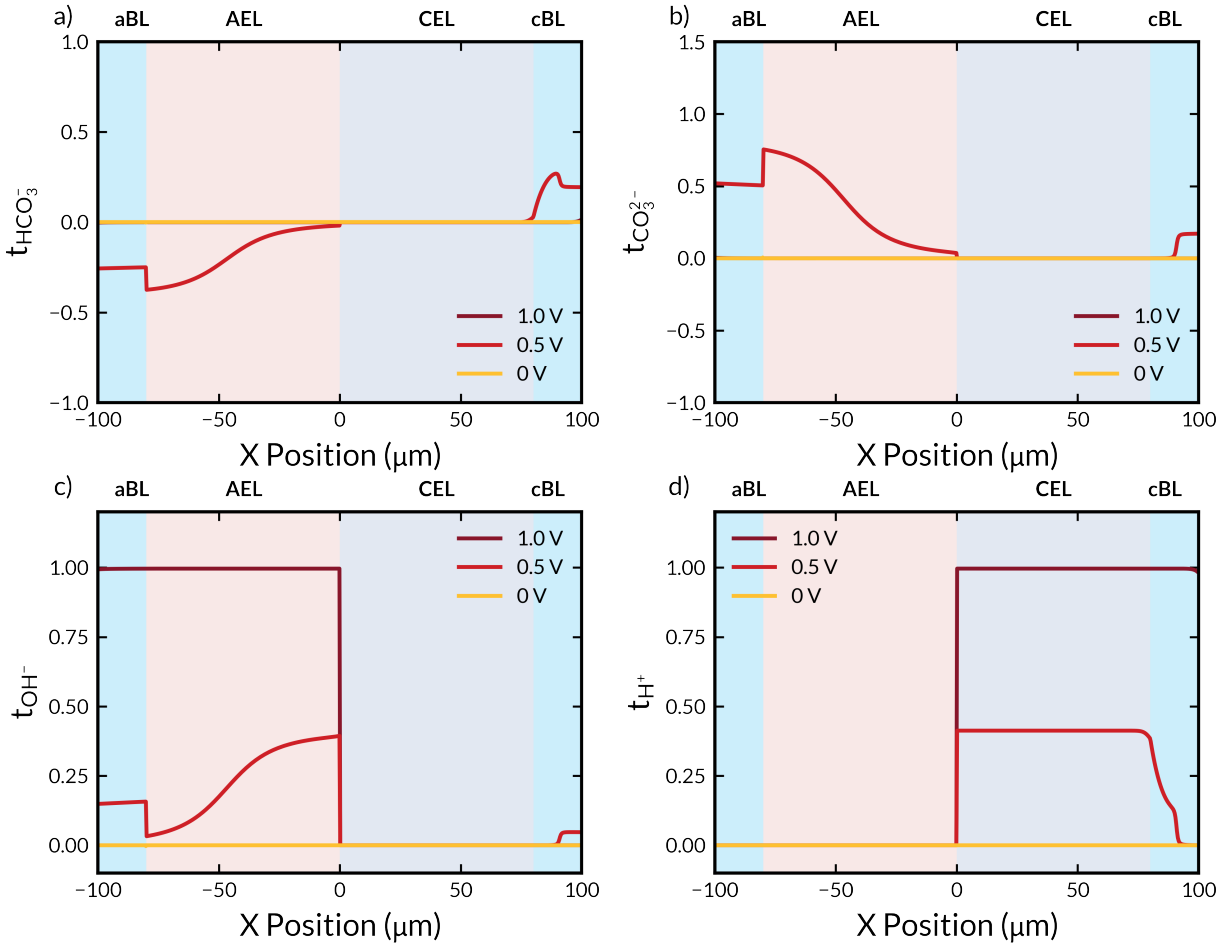

Figure S34: Simulated transference number profiles of **(a)** HCO_3^-, **(b)** CO_3^{2-}, **(c)** OH^-, and **(d)** H^+ within a BPM immersed in simulated seawater at applied membrane voltages of 0 V, 0.5 V, and 1.0 V.

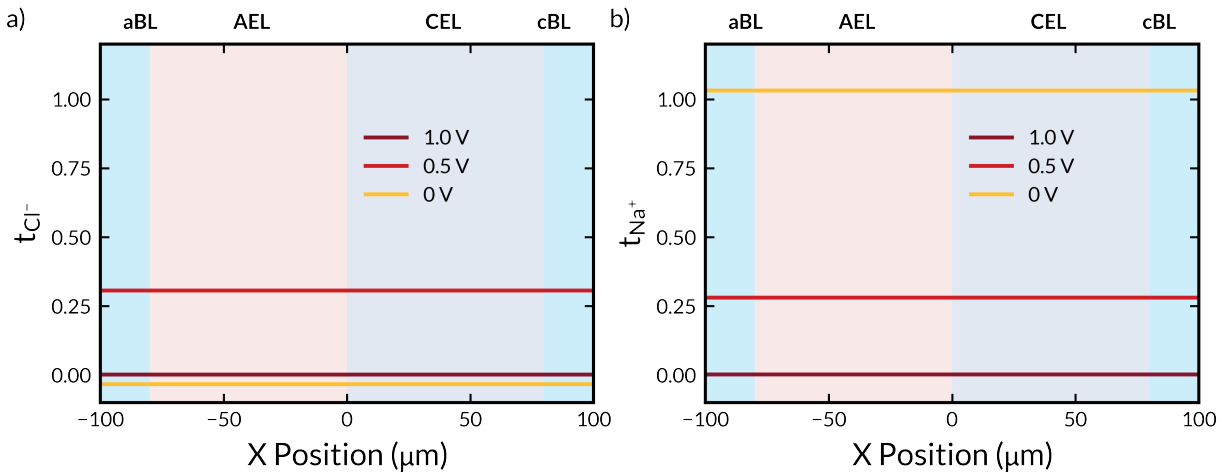

Figure S35: Simulated effective transference number profiles of **(a)** Cl^-, **(b)** Na^+ within a BPM immersed in simulated seawater at applied membrane voltages of 0 V, 0.5 V, and 1.0 V.

S15: Water Dissociation Efficiency of BPM in 1 M $KHCO_3$ and Simulated Seawater

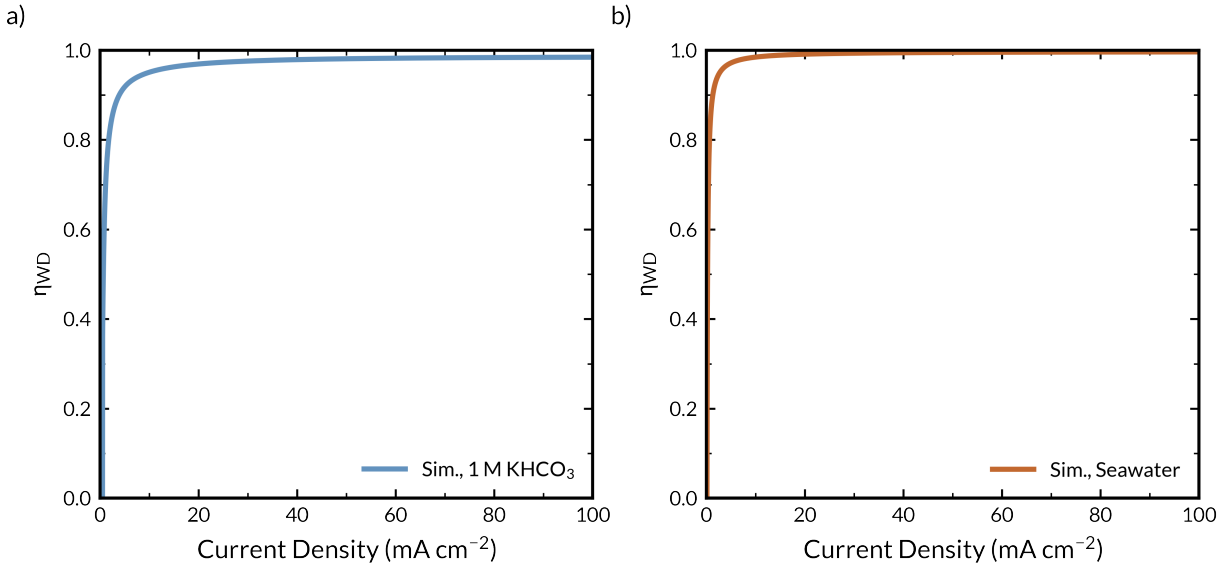

Figure S36: Water dissociation efficiency (defined as the integration of the rate of WD in the WD CL divided by the total current density) as a function of applied membrane potential for a BPM immersed in **(a)** 1 M $KHCO_3$ and **(b)** simulated seawater.

S15.1 Definition of Water Dissociation Efficiency

The water dissociation efficiency is calculated using the following expression.

$$\eta_{WD} = \frac{F \int_{L_{CL}} R_1 dx}{i_{BPM}} \quad \text{(S42)}$$

where i_{BPM} is defined as the total ionic current passed through the BPM.

S16: Zoomed Inset of Coulombic Efficiency and Energy Intensity for $i < 10$ mA cm^{-2}

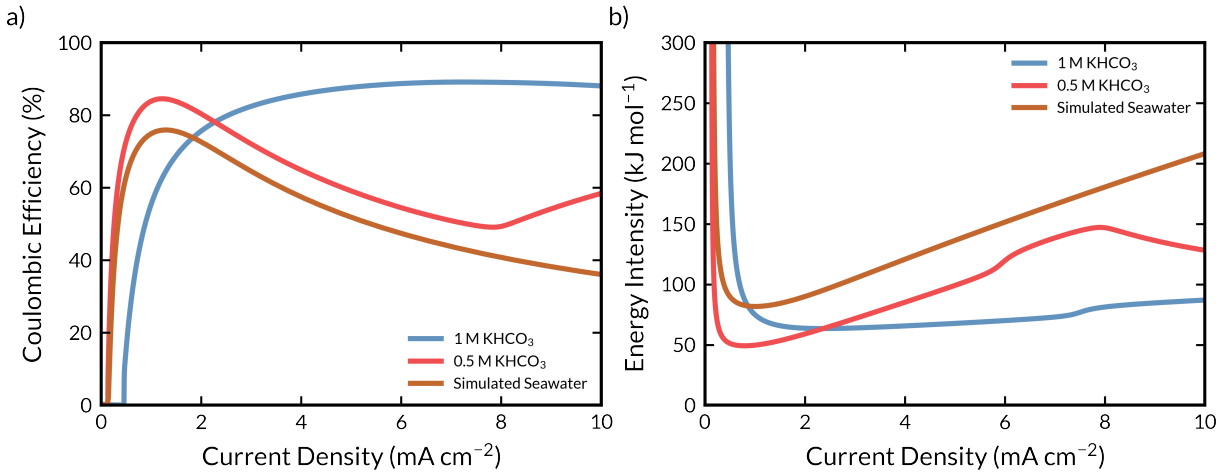

Figure S37: Simulated **(a)** coulombic efficiency and **(b)** energy intensity of CO_2 regeneration via BPM-ED for EMCC from 1 M and 0.5 M $KHCO_3$ as well as for DOC in simulated seawater for $i <$ 10 mA cm^{-2}.

S17: Note on Inflection Point in CO_2 Regeneration Rate

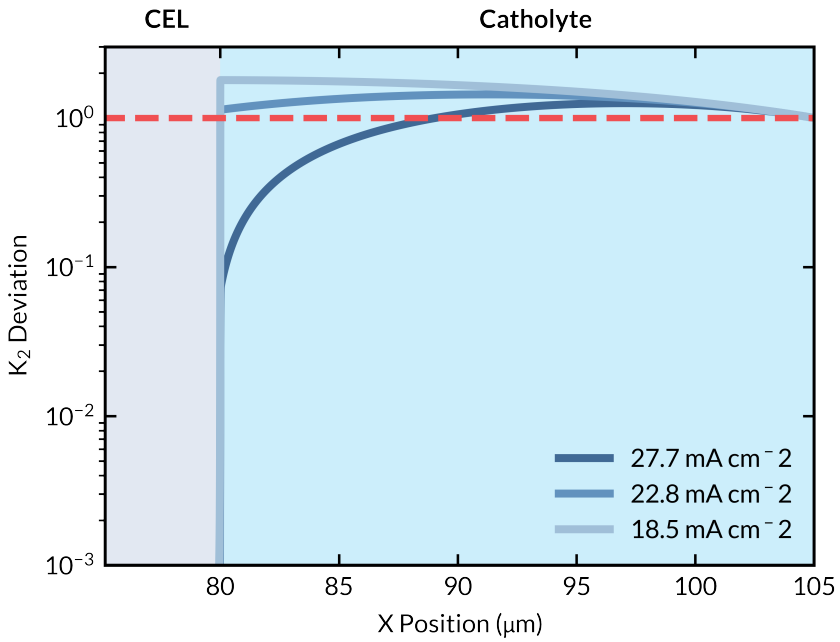

Figure S38: Equilibrium deviation for CO_2 regeneration within the catholyte as a function of position and applied current density.

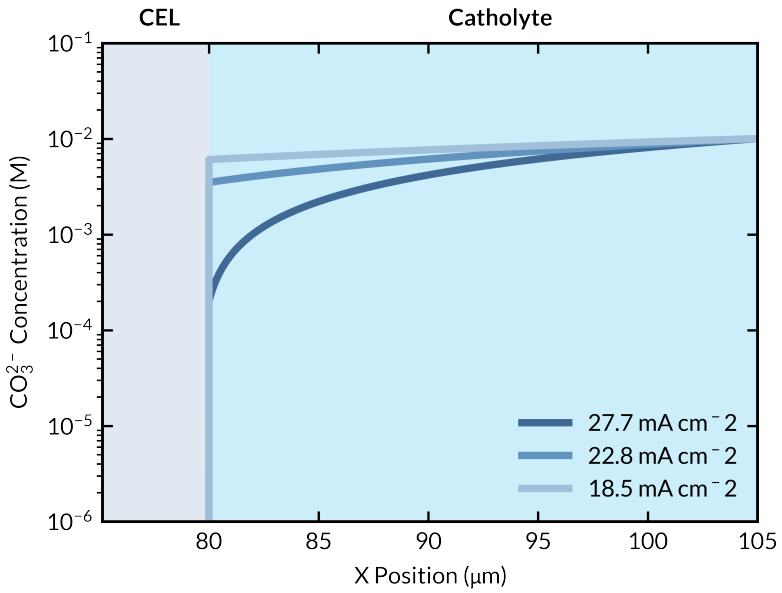

Figure S39: Local concentration of CO_3^{2-} within the catholyte as a function of position and applied current density.

S17.1 Supplementary Note on Catholyte Equilibrium and Inflection Point in CO_2 Regeneration Rate Curve

The inflection point observed in the rate of CO_2 efflux is an interesting phenomenon, and can be described by analyzing the equilibrium of reaction (2) in the catholyte (**Figure S31**), as well as the local CO_3^{2-} concentration (**Figure S32**). For current densities below the inflection point (i < 25 mA cm^{-2}), the equilibrium of reaction (2), is approximately in equilibrium and not serving as a net-generator of CO_2. This is due to the presence of CO_3^{2-} within the catholyte. CO_3^{2-} anions consume water-dissociation-generated H^+ to form HCO_3^- by reaction (3), which in turn affects the equilibrium of reaction (2). However, beyond the inflection point (i > 25 mA cm^{-2}), CO_3^{2-} is almost completely consumed within the catholyte, and reaction (2) is driven in the direction of CO_2 generation due to a surplus of H^+ present at the CEL|cBL interface. Essentially, the inflection in the coulombic efficiency and energy intensity are due to the competitive reaction of H^+ with CO_3^{2-}. Once all CO_3^{2-} in the catholyte is consumed, the H^+ generated by water dissociation can be used for CO_2 regeneration.

S18: Fluxes and Efficiencies of Sorbent Regeneration within the AEL

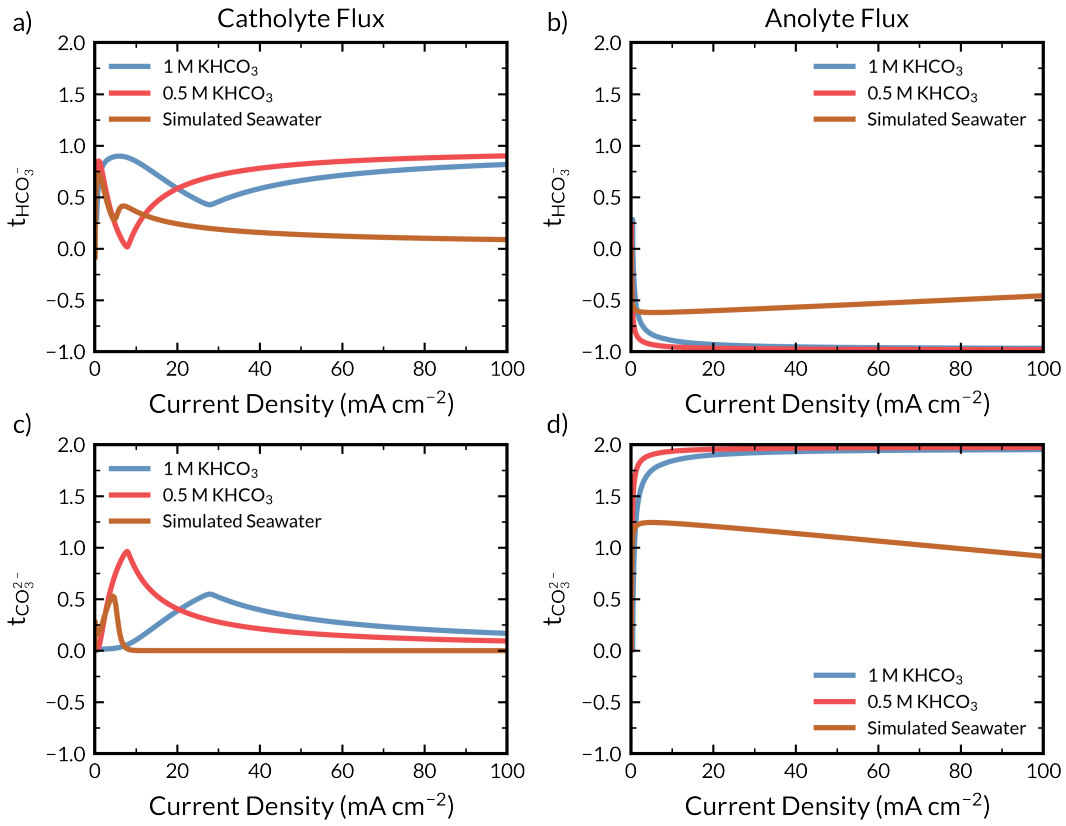

Figure S40: Flux of **(a,b)** HCO_3^- and **(c,d)** CO_3^{2-} out of the **(a,c)** catholyte and **(b,d)** anolyte as a function of applied BPM current density. The coulombic efficiency of sorbent regeneration is related to the transference number of CO_3^{2-} at the anolyte boundary because when the transference number for CO_3^{2-} is 2, then all the ionic current within the AEL is going towards the conversion of HCO_3^- to CO_3^{2-}.

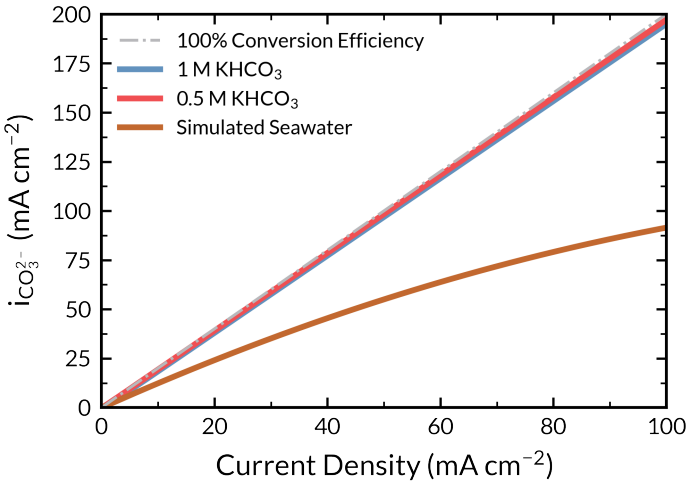

Figure S41: Current density of CO_3^{2-} out of the anolyte boundary as a function of applied current density.

S19: Effect of pH Gradient Operation on Polarization Curve and Efficiencies

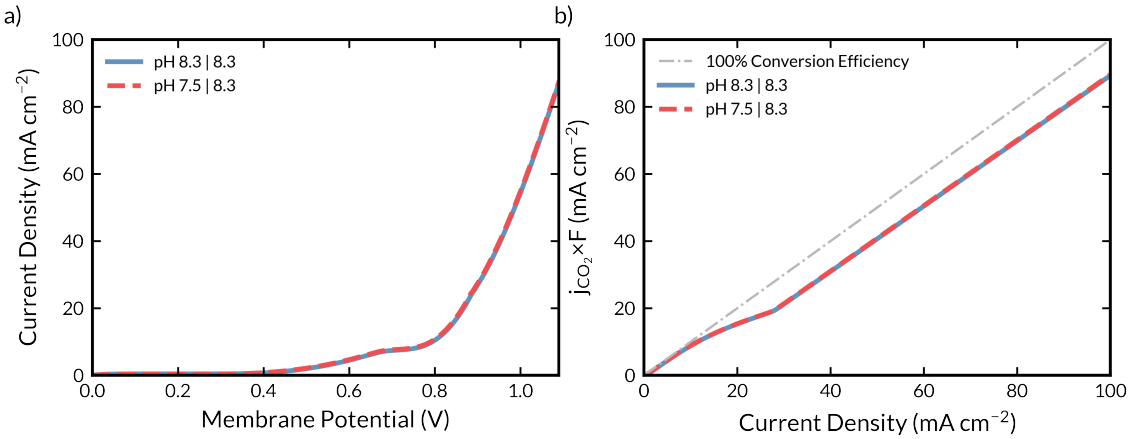

Figure S42: Effect of pH gradient operation on **(a)** polarization curve and **(b)** CO_2 conversion coulombic efficiency.

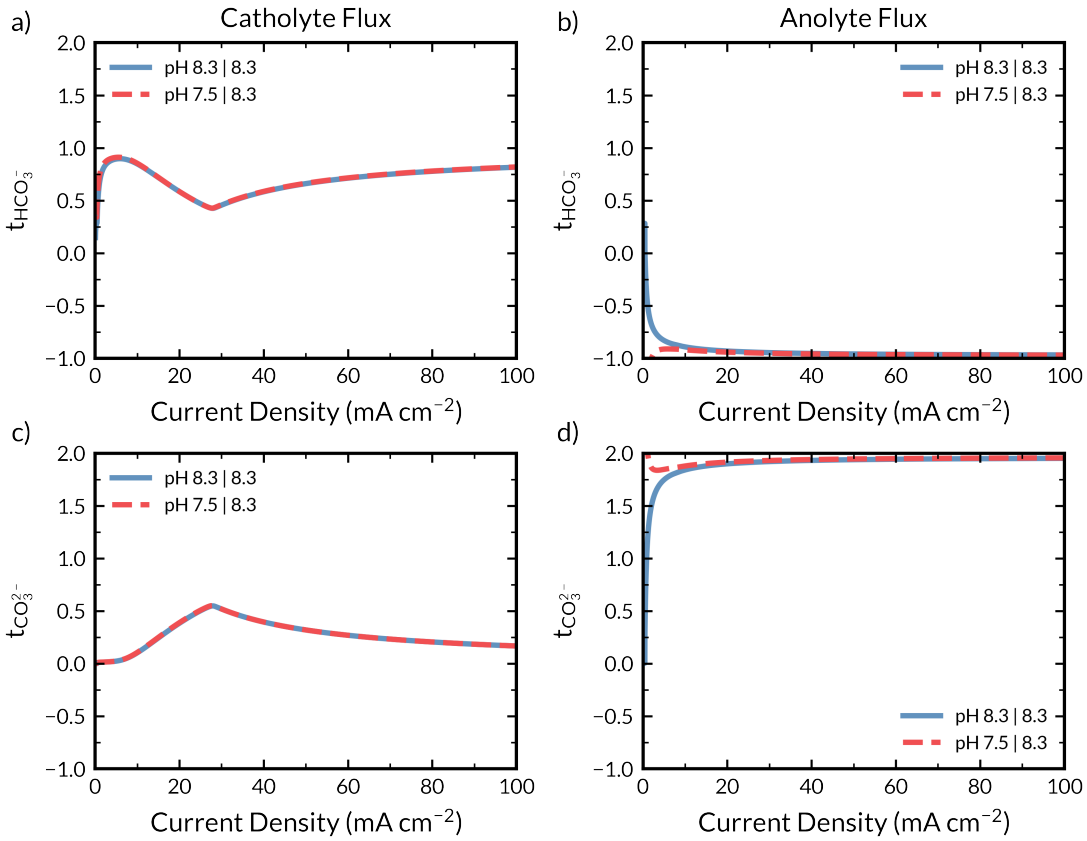

Figure S43: Effect of pH gradient operation on transferences of fluxes of (bi)carbonates into or out of the **(a,c)** catholyte, and **(b,d)** anolyte.

S20: Effect of Boundary-Layer Thickness on Polarization Curve and CO_2 Bubbling

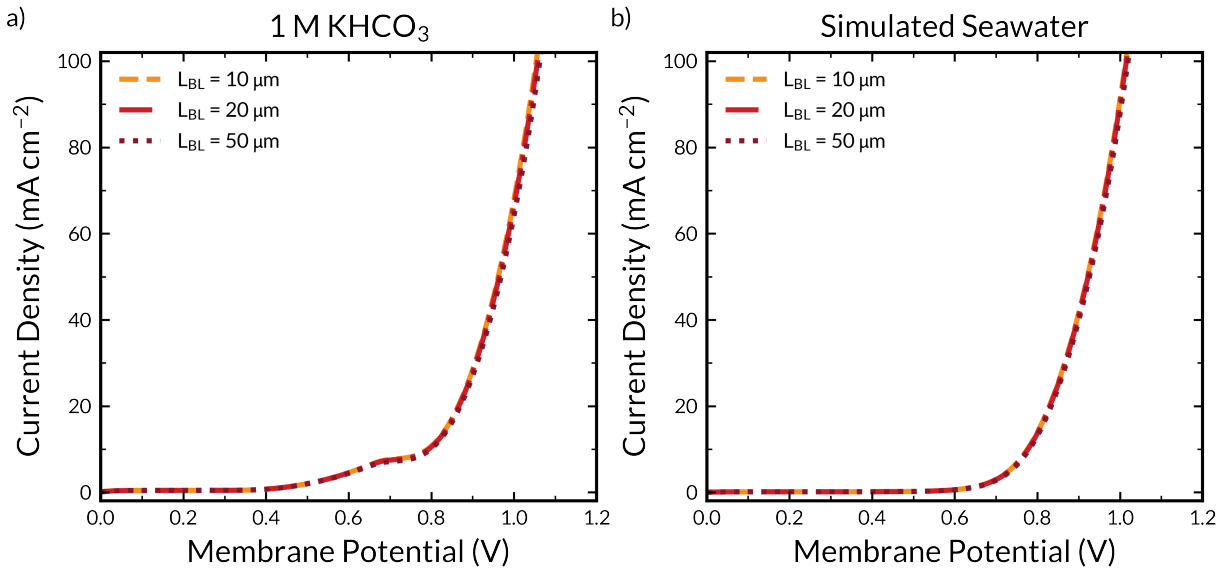

Figure S44: Effect of boundary-layer thickness on the BPM polarization curve (with bubble coverage effects deconvoluted) for a BPM immersed in **(a)** 1 M $KHCO_3$ and **(b)** simulated seawater.

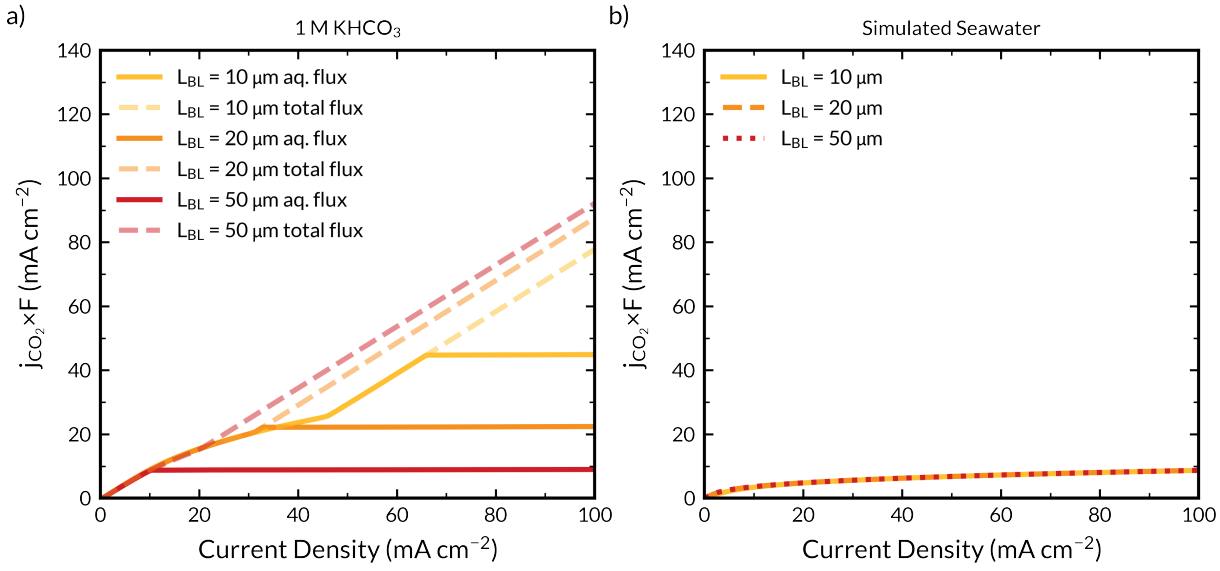

Figure S45: Effect of boundary-layer thickness on the catholyte CO_2 flux for a BPM immersed in **(a)** 1 M $KHCO_3$ and **(b)** simulated seawater.

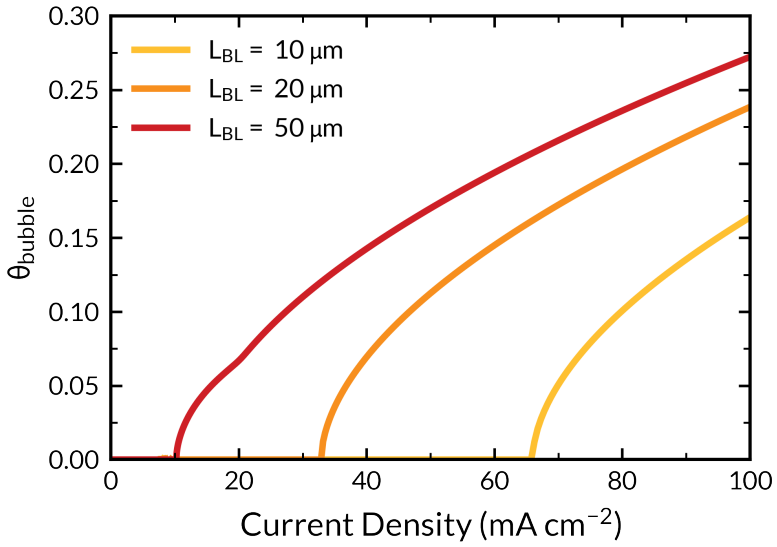

Figure S46: Effect of boundary layer thickness on the simulated bubble coverage on the CEL.

S21: Experimental Analysis of Flowrate Effects

S22.1 Supplementary Experimental Methods for Flowrate Experiments

Commercial Fumasep BPMs were used for all experiments. All tests were performed in our custom electrodialysis flow cell described in **Section 2.2**, flowing 1 M $KHCO_3$ (unless otherwise stated). Stirring in the acid and base chambers was implemented for all experiments to minimize mass transport effects other than flow. Chronopotentiometry measurements were stepped from 0 to 100 mA cm^{-2}, holding for 2 min at each current and measuring the resulting voltage across the BPM. Average and standard deviation of the voltage at each current step with the calculated for the final 60 seconds of each step. The standard deviation of the voltage was then used as a metric to determine the amount of bubbling at each current.

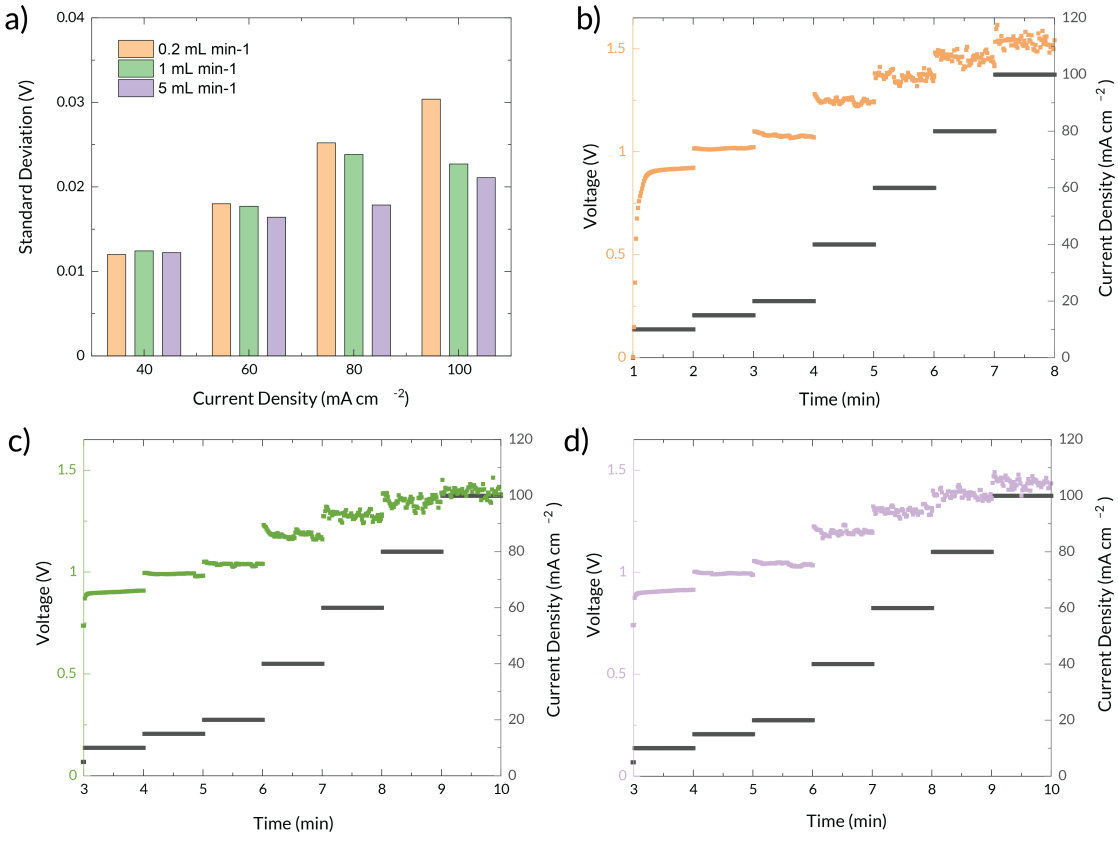

Figure S47: Experimental measurements of bubbling at CEL surface of Fumasep BPM with varying flow rate. a) Comparison of the current density at which bubbling begins based on flow

rate through the cell, *via* standard deviation of measured voltage. Voltage vs. time for current step measurements at b) 0.2 mL min^{-2}, c) 1 mA cm^{-2}, and d) 5 mA cm^{-2}.

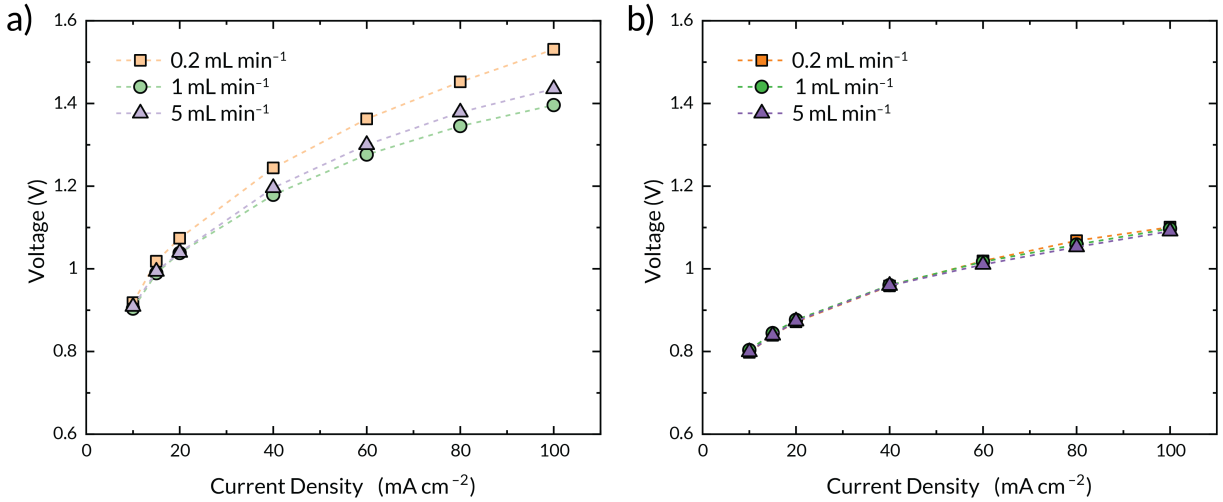

Figure S48: Polarization curves depicting average voltage vs. current density for Fumasep tested in a) 1 M $KHCO_3$ and b) 0.5 M NaCl.

S22: Effect of Bubbling on Polarization Curve and CO_2 Generation

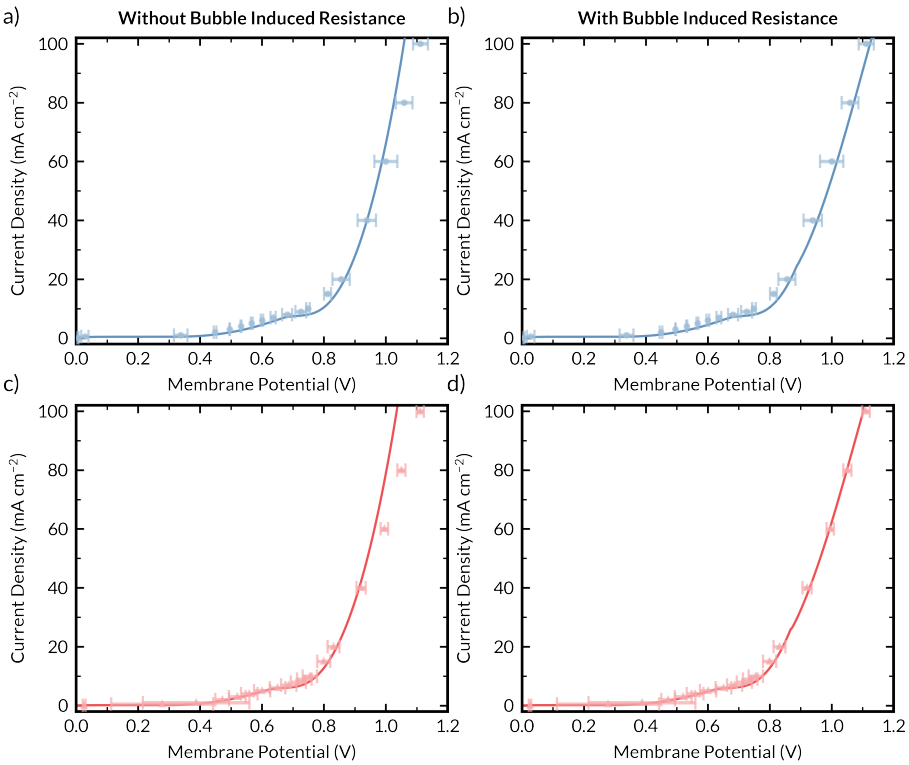

Figure S49: Impact of bubble induced resistances on BPM polarization curves for BPMs immersed in **(a,b)** 1 M $KHCO_3$ and **(c,d)** 0.5 M $KHCO_3$.

S23: Impact of Divalent Cations

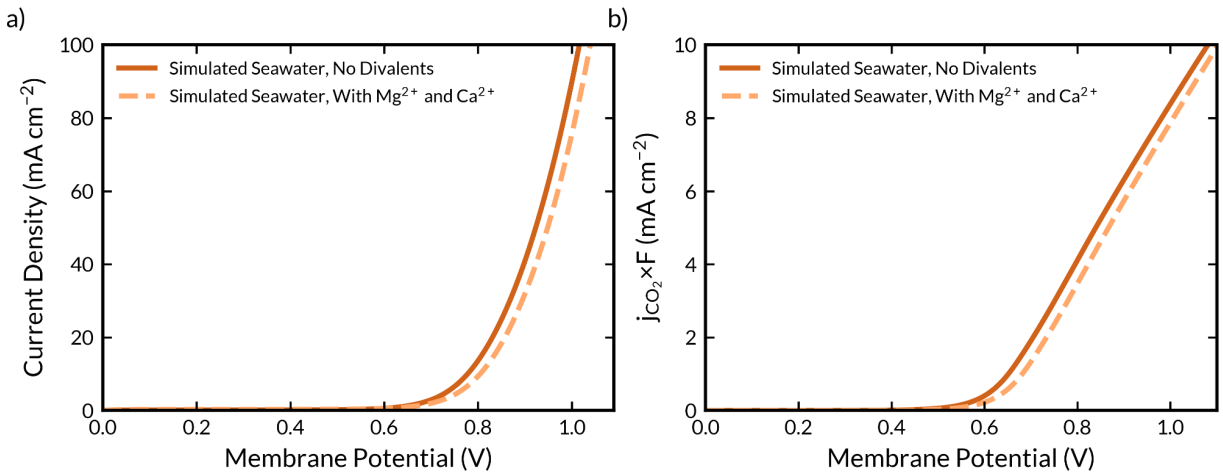

Figure S50: Effect of divalent cations on **(a)** polarization behavior and **(b)** CO_2 regeneration rate for a BPM immersed in seawater.

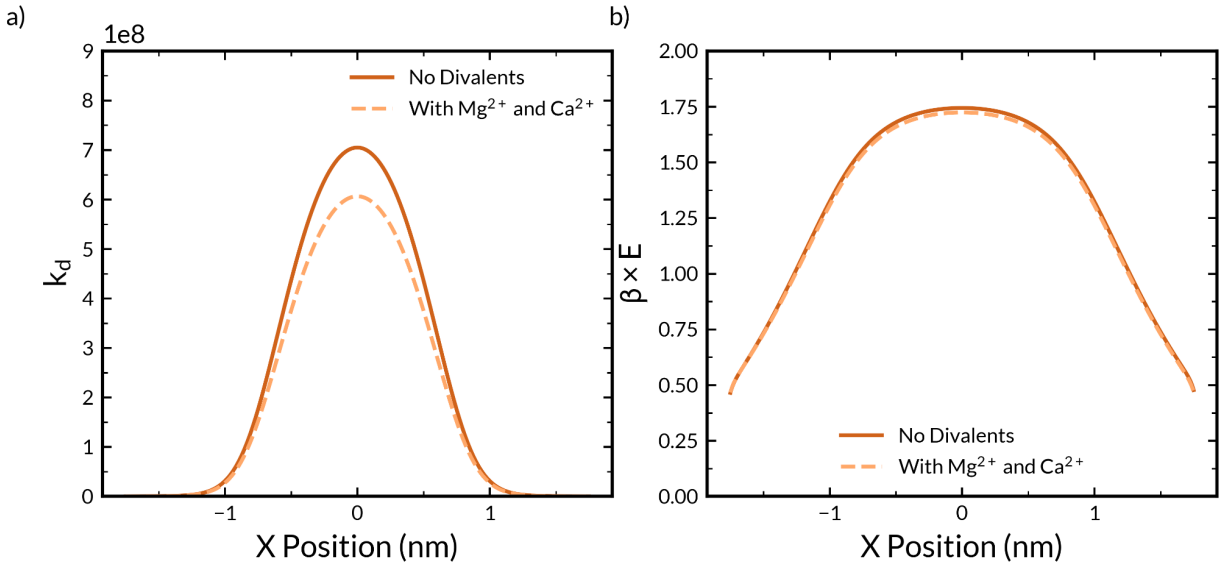

Figure S51: Catalyst layer **(a)** water dissociation rate and **(b)** electric field for the BPM immersed in seawater with and without divalent cations.

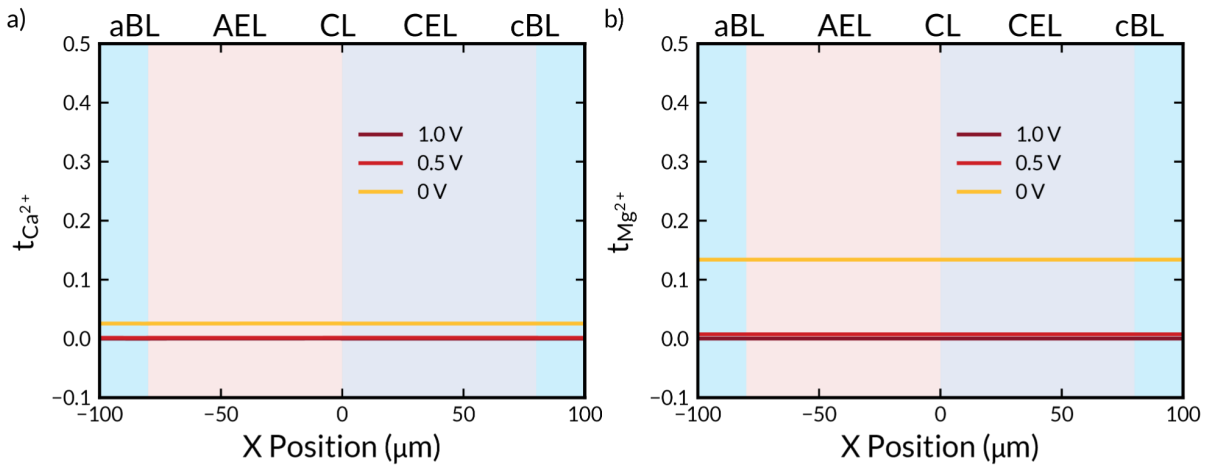

Figure S52: Transference number profiles **(a)** Ca^{2+} and **(b)** Mg^{2+} at transmembrane potentials of 0, 0.5, and 1.0 V for BPMs immersed with seawater containing divalent cations.

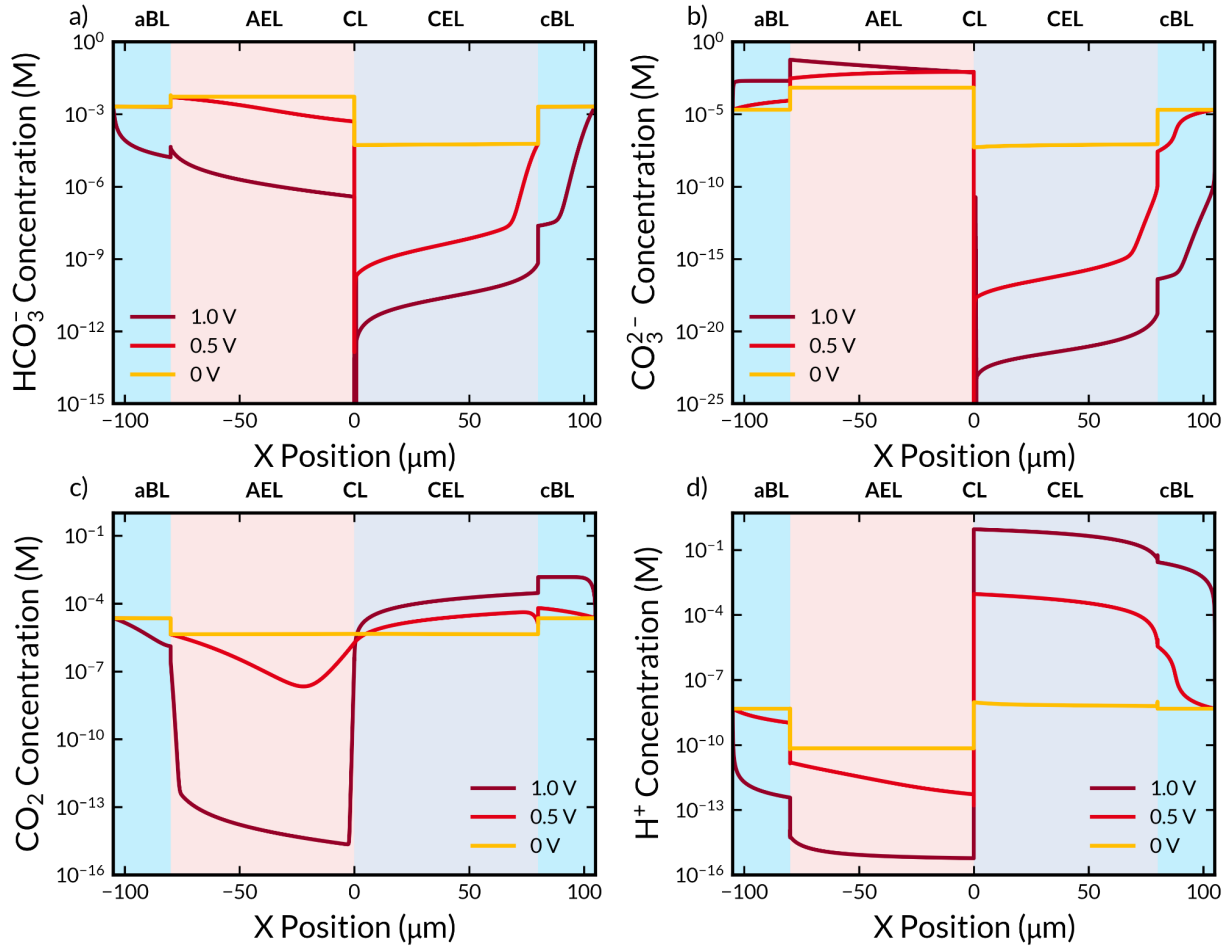

Figure S53: Concentration profiles **(a)** HCO_3^-, **(b)** CO_3^{2-}, **(c)** CO_2, and **(d)** H^+ at transmembrane potentials of 0, 0.5, and 1.0 V for BPMs immersed with seawater containing divalent cations.

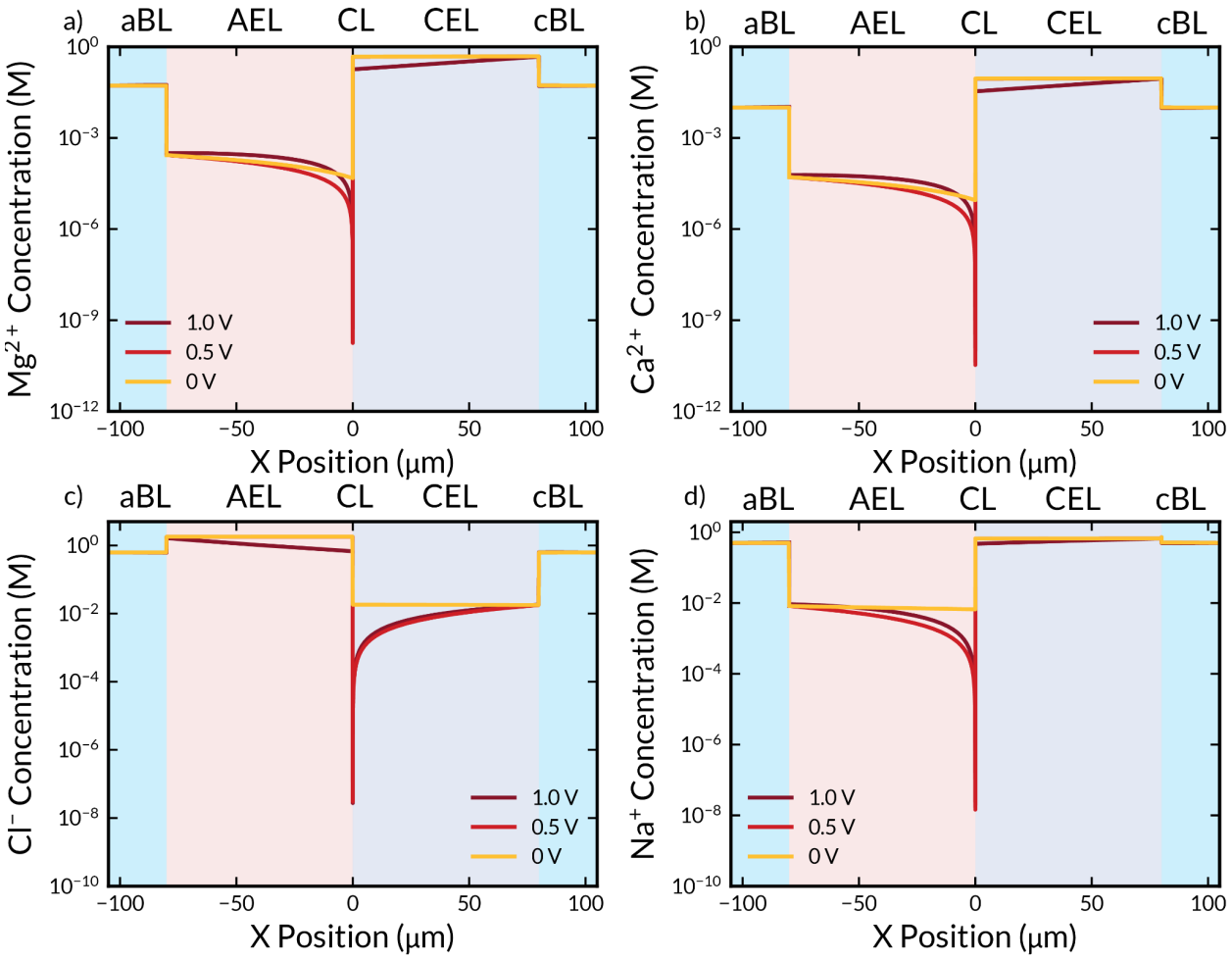

Figure S54: Concentration profiles **(a)** Mg^{2+}, **(b)** Ca^{2+}, **(c)** Cl^-, and **(d)** Na^+ at transmembrane potentials of 0, 0.5, and 1.0 V for BPMs immersed with seawater containing divalent cations.

S23.1 Supplementary Note on Impact of Ions on Terminal Electrode Performance

At the terminal anode, the presence of Cl^- ions could lead to Cl_2 evolution (ClER) at the anode, because Cl_2 evolution, while more thermodynamically unfavorable than O_2 evolution (OER), is more kinetically facile. Fortunately, the selectivity of OER over ClER is highly pH dependent, with OER being nearly perfectly selective at high pH.[22] Correspondingly, if one ensures that the anode feed is sufficiently alkaline, the ClER reaction can be suppressed. Furthermore, BPMs placed in reverse bias to alkalinize the anode have been shown to be successful in suppressing anodic ClER, further justifying their implementation in processes with impure feeds.[23] At the terminal cathode, $Mg(OH)_2$ or $Ca(OH)_2$ scaling can also be prevented by implementing a BPM in reverse bias adjacent to the cathode. WD-generated H^+ ensure the cathode environment remains sufficiently acidic as to circumvent formation of solid hydroxides.[24] Correspondingly, BPMs possess great promise for both performing capture, as well as for enhancing durability in electrochemical systems with impure feeds. These durability effects are beyond the scope of the present work and will be a deep area of future exploration.

S24: Sensitivity Analysis

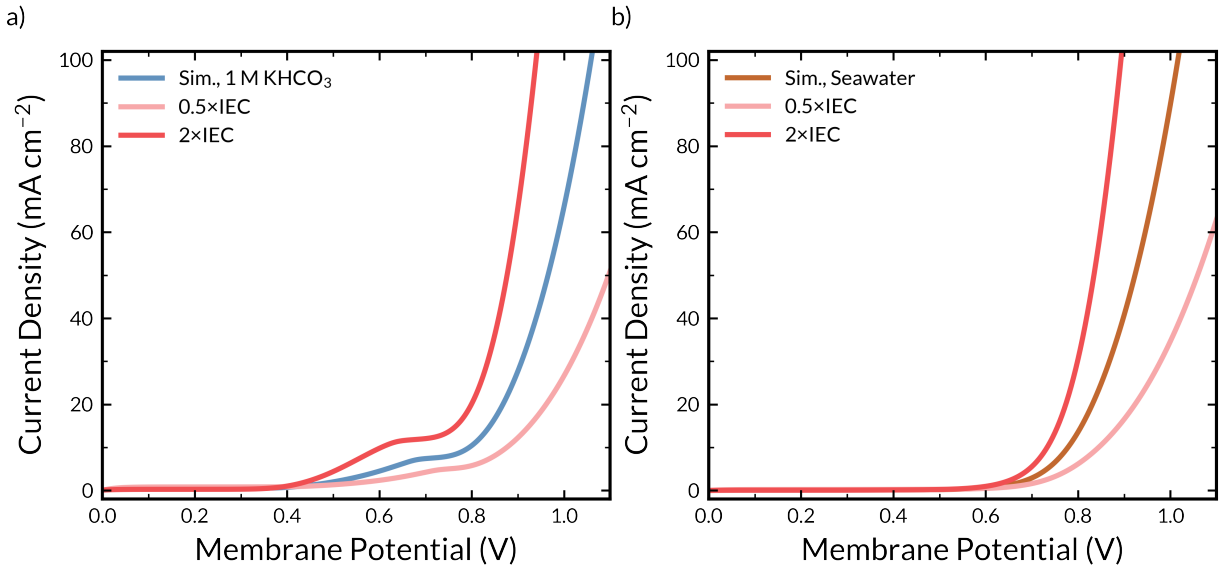

Figure S55: Effect of ion-exchange capacity on BPM polarization curve for a BPM immersed in **(a)** 1 M $KHCO_3$ and **(b)** simulated seawater.

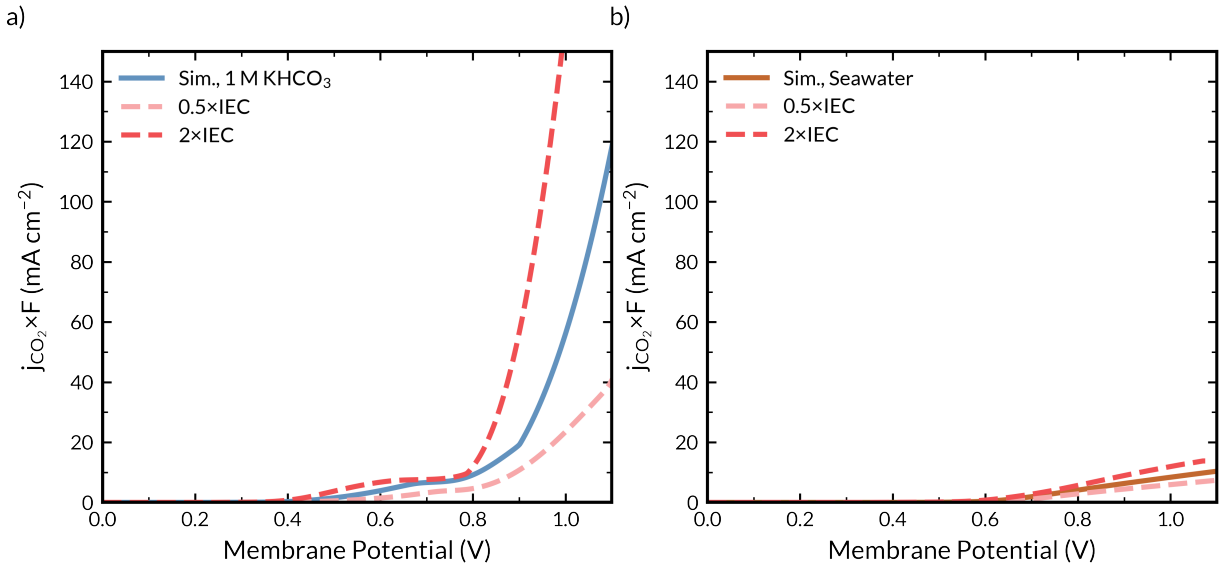

Figure S56: Effect of ion-exchange capacity on catholyte CO_2 efflux for a BPM immersed in **(a)** 1 M $KHCO_3$ and **(b)** simulated seawater.

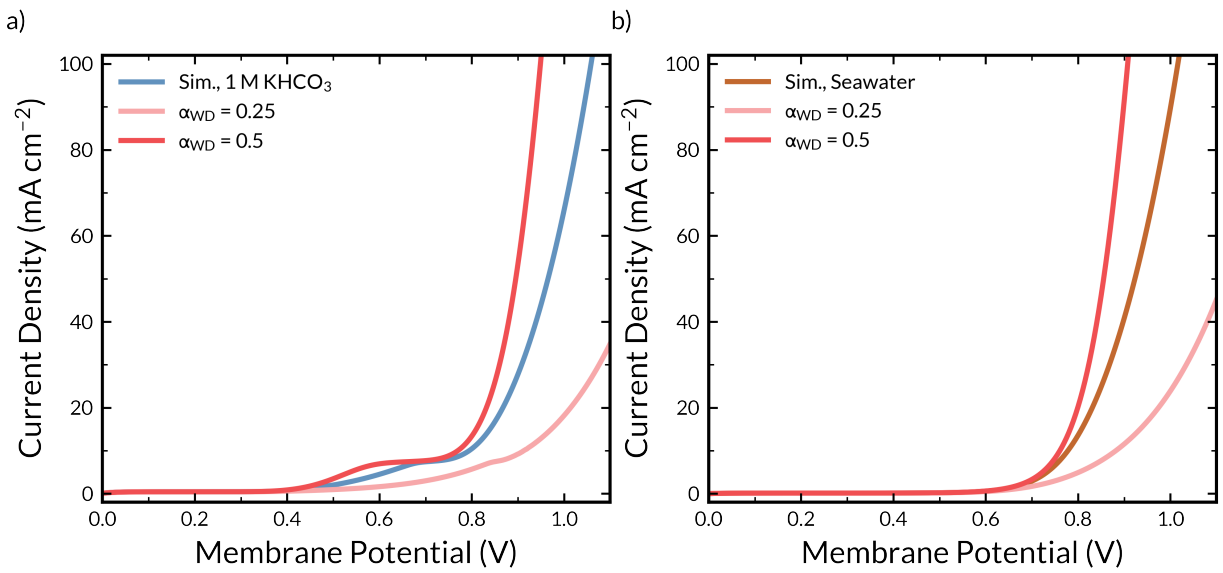

Figure S57: Effect of water dissociation transfer coefficient on BPM polarization curve for a BPM immersed in **(a)** 1 M $KHCO_3$ and **(b)** simulated seawater.

S24.1 Supplementary Note on Sensitivity to Membrane Thickness and Water Uptake

Sensitivity analysis was also performed to discern the impacts of CEL or AEL thickness. Thickness sensitivity is particularly relevant given recent studies showing that thinning one of the membrane layers is vital to facilitate water transport to the junction and enable high current densities (> 500 mA cm^{-2}).[7,25] As seen in **Figure S58**, decreasing the thickness of the AEL increases the performance for the BPM for DAC operated in 1 M $KHCO_3$, by increasing the rate of HCO_3^- dissociation. HCO_3^- dissociation is enhanced with thinner AELs because of improved delivery of HCO_3^- to the high field region of the BPM. However, while the thinner AEL improves the rate of CO_2 recovery by providing greater H^+ flux *via* bicarbonate dissociation, greater K^+ crossover occurs because the thin AEL is less capable of excluding K^+ cations thermodynamically from the BPM. For the

case of the thin CEL in DAC systems, the performance is only slightly enhanced, due to reduced ohmic losses through the thinner CEL. For DOC systems immersed in seawater, the results are similar, with the caveat that the concentration of HCO_3^- in seawater is too dilute to observe improvements in HCO_3^- dissociation. Thinning the individual layers of the BPM improves performance by reducing ohmic losses. However, these reduced ohmic losses come at the expense of increased co-ion crossover due to poorer electrostatic exclusion of co-ions from the BPM.

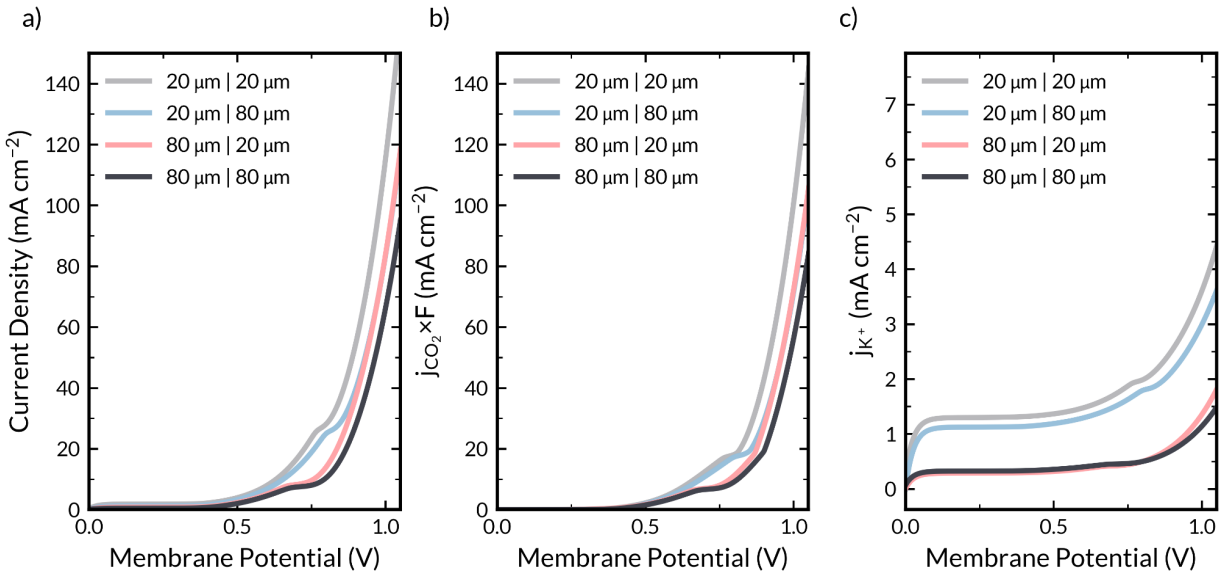

Figure S58: Effect of AEL or CEL thickness on **(a)** BPM polarization curve **(b)** CO_2 regeneration rate, and **(c)** K^+ crossover for a BPM immersed in 1 M $KHCO_3$ electrolyte.

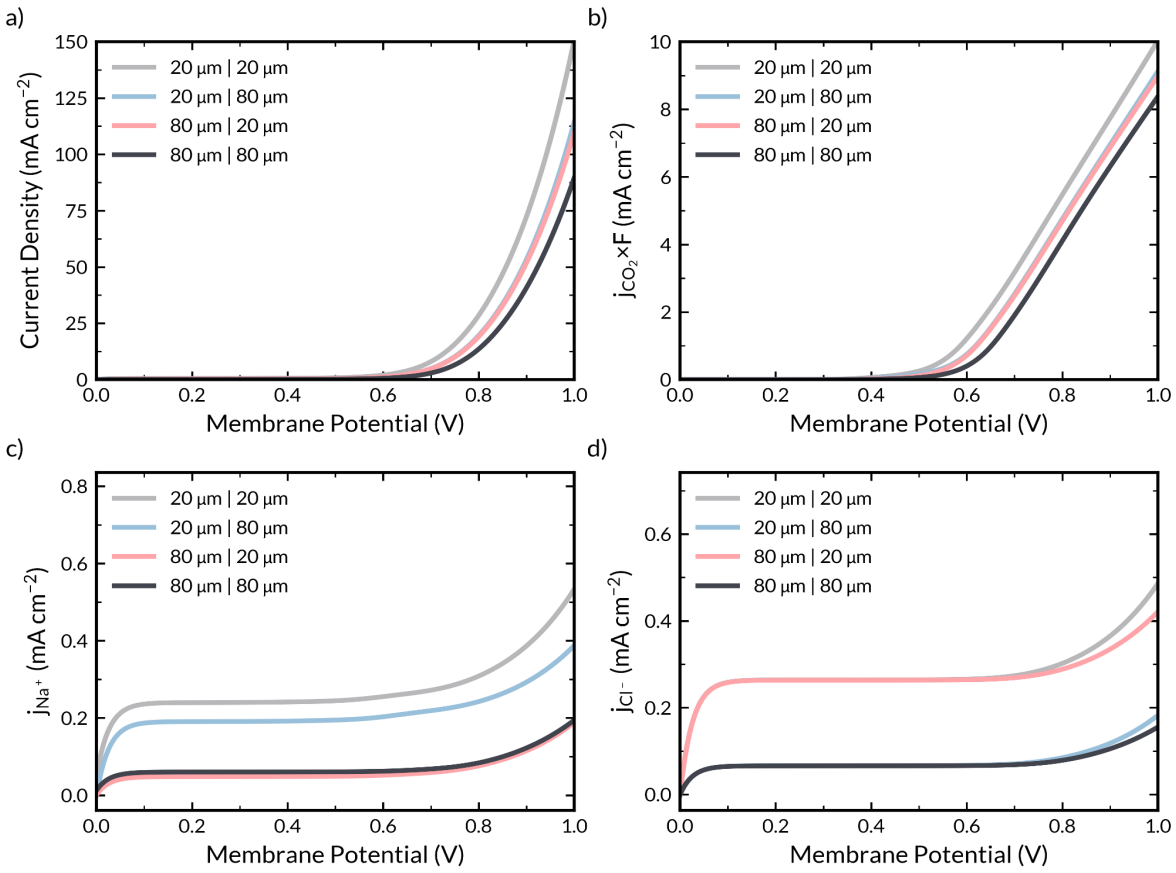

Figure S59: Effect of AEL or CEL thickness on **(a)** BPM polarization curve **(b)** CO_2 regeneration rate, and **(c)** Na^+ crossover, and **(d)** Cl^- crossover for a BPM immersed in simulated seawater.

An alternative method for improving water transport is to increase the BPM water uptake (moles of water per moles of fixed charge).[26,27] Fumasep has notably low water uptake ($\lambda = 9$)[28] compared to Nafion ($\lambda = 21$)[29] or Piperion ($\lambda = 20$)[30], membranes that have been commonly employed in next-generation BPMs.[7,31,32] Simulations with BPMs containing water uptakes 2× that of Fumasep ($\lambda = 18$), on par with Nafion or Piperion, show that enhanced water uptake results in marginal improvements in polarization performance, reducing ohmic losses in both DAC and DOC electrolytes (**Figures S60-61**), as well as enhancing the rate of HCO_3^- dissociation in systems with high concentrations of HCO_3^-.

However, as with modulating thickness, enhancements from improved water uptake come at the cost of increased co-ion leakage. These results indicate that there is a tradeoff between BPM energy efficiency and co-ion leakage, similar to the throughput-selectivity tradeoff observed in reverse osmosis membranes.[33]

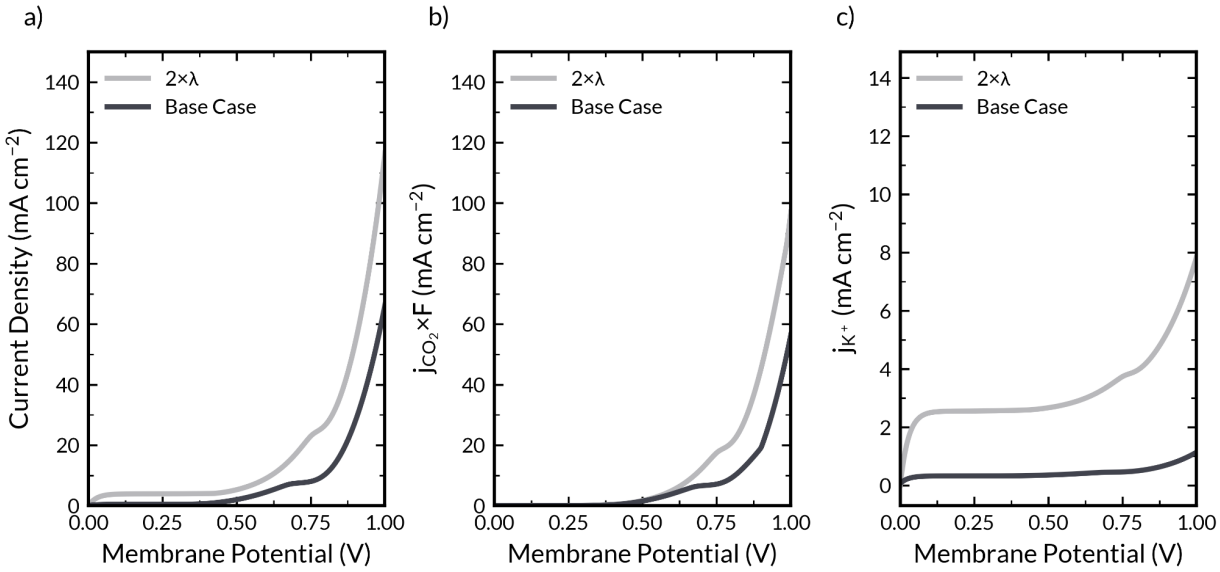

Figure S60: Effect of BPM water uptake on **(a)** BPM polarization curve **(b)** CO_2 regeneration rate, and **(c)** K^+ crossover for a BPM immersed in 1 M $KHCO_3$ electrolyte.

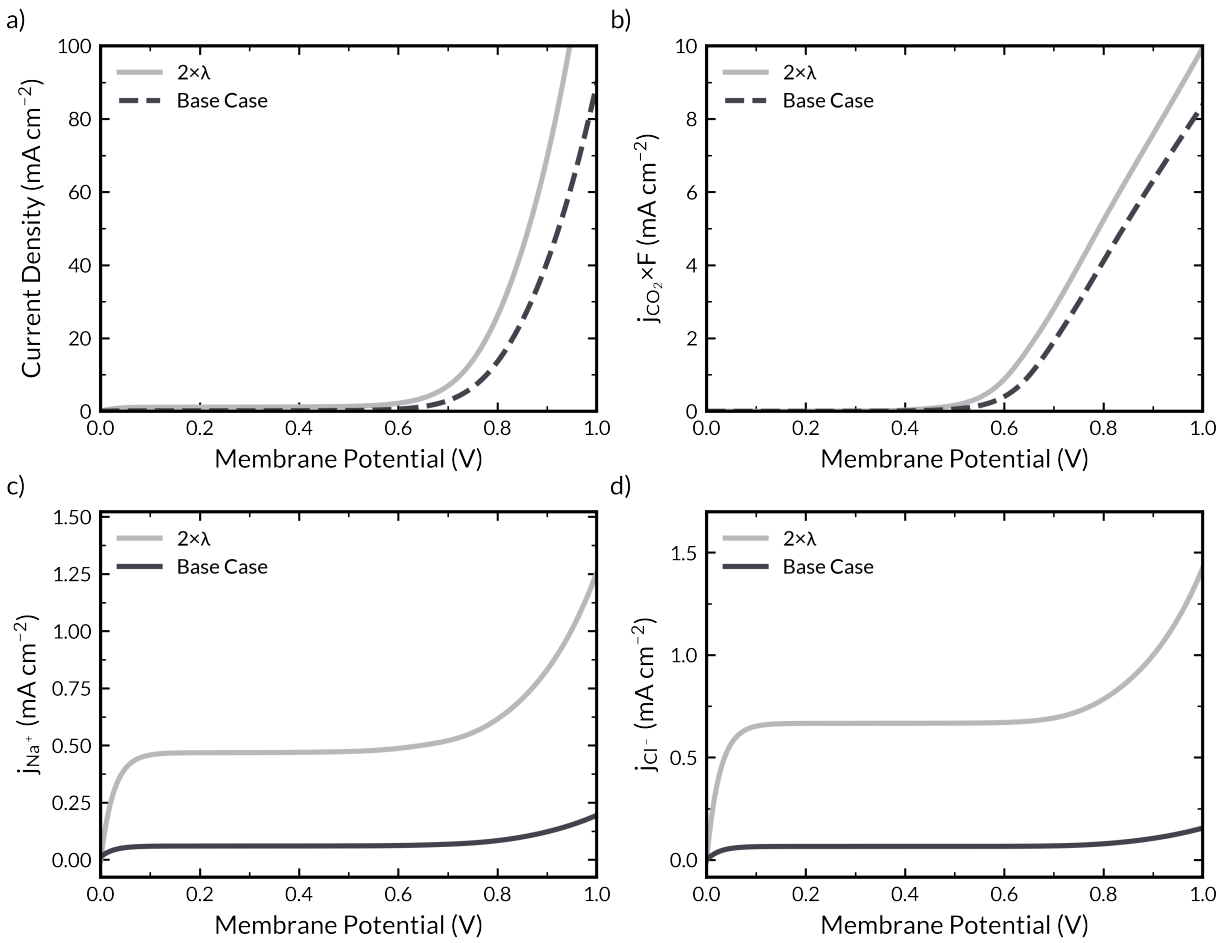

Figure S61: Effect of BPM water uptake on **(a)** BPM polarization curve **(b)** CO_2 regeneration rate, and **(c)** Na^+ crossover, and **(d)** Cl^- crossover for a BPM immersed in simulated seawater.

S24.2 Supplementary Note on "Optimal BPM" Simulations

To develop a sensitivity analysis for an "Optimal BPM", the model was fit to polarization data collected using a recently developed freestanding BPM with a 3D-junction capable of achieving high WD rates at low applied overpotentials.[34] The polarization data as originally reported was IR-corrected, but the model captures IR losses in the BPM and electrolyte, so the IR correction in the experimental data was removed for comparison. The Pintauro BPM is reported to have a greater fixed charge of approximately 5 M, so the fixed charge in each layer of the simulated optimal BPM was multiplied by a factor of 2,

and α_{WD} was set to a value of 0.5 to account for the advanced 3D-junction WD catalyst. It is important to note that other membrane properties (thickness, water uptake, *etc.*) were not changed due to those parameters not having substantial effect on energy requirements for the BPM, along with a lack of measured transport properties, water uptake isotherms, *etc.* for the novel BPM. Thus, while the "Optimal BPM" was fit to have near identical polarization behavior to the reported BPM by changing IEC and α_{WD}, all other properties are that of the Fumasep BPM, so it is not a perfect 1:1 comparison. Nonetheless, developing simulations matching the current-voltage behavior is more than sufficient for the purposes of the sensitivity analysis and facilitates a theoretical estimate of the floor for energy requirements when employing state-of-the-art BPMs.

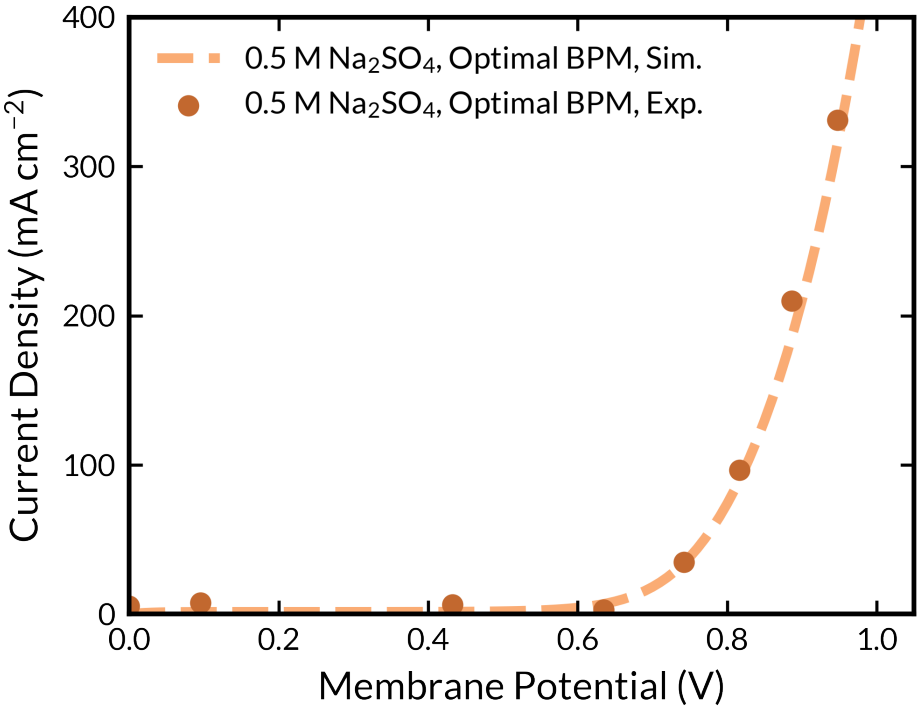

Figure S62: Comparison of **(a)** "optimal BPM" as simulated and **(b)** experimental polarization curve collected by Pintauro *et al.*[34] for a BPM with a 3D-junction operating in 0.5 M Na_2SO_4.

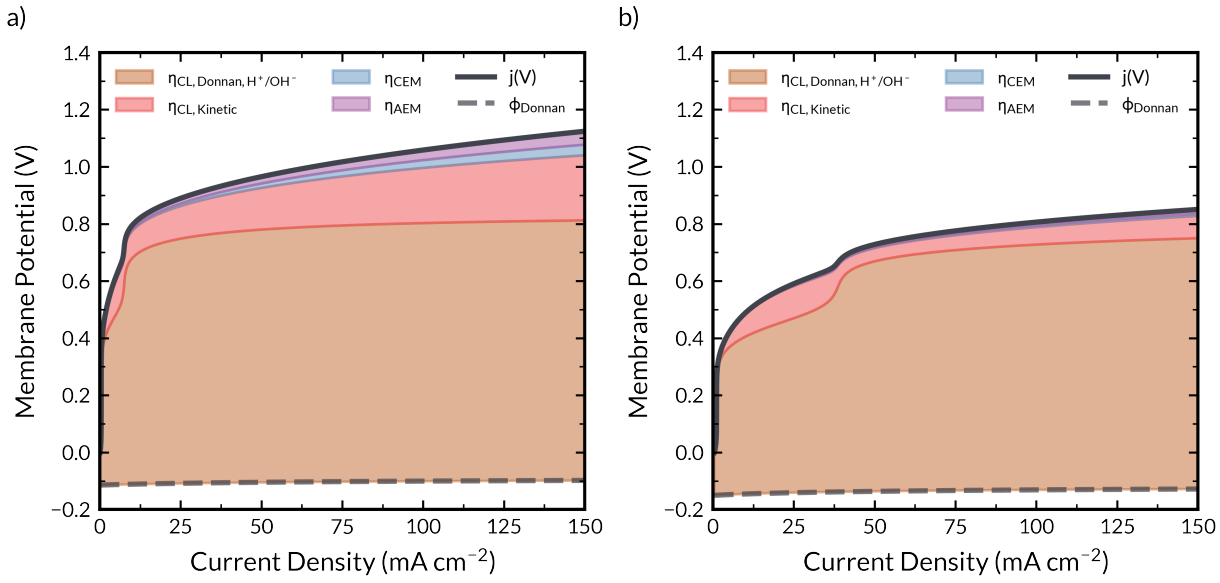

Figure S63: Applied-voltage breakdown as simulated for **(a)** commercial Fumasep BPM, and **(b)** optimal BPM.

S25: Theoretical Analysis of Performance in a BPM-ED Stack

Calculations of the energy intensity and total cell potential were calculated for both the Fumasep and Optimal BPM operating at 100 mA cm^{-2}. The BPM potential and Coulombic efficiencies are determined from the simulation for each of these BPMs as follows:

Table S6: List of calculated voltages and efficiency from continuum model that are employed in the process-level calculation.

PARAMETER	VALUE	UNITS
$\boldsymbol{V_{BPM,Fumasep}(j = 100\ [mA\ cm^{-2}])}$	1.059	V
$\boldsymbol{V_{BPM,Optimal}(j = 100\ [mA\ cm^{-2}])}$	0.806	V
$\boldsymbol{\eta_{Coulomb,Fumasep}(j = 100\ [mA\ cm^{-2}])}$	0.893	A. U.

$\boldsymbol{\eta_{Coulomb,Optimal}(j = 100\ [\mathrm{mA\ cm^{-2}}])}$	0.879	A. U.

The performance of the overall BPM stack can then be calculated by the following expression.

$$V_{stack} = (V_{anode} - V_{cathode} + n\bar{V}_{ohmic} + nV_{BPM}) \quad \text{(S43)}$$

where V_{anode} and $V_{cathode}$ are the potentials of the anode and cathode, respectively, $\bar{V}_{ohmic}$ is the ohmic loss per unit cell, and V_{BPM} is the potential drop through the BPM as shown in **Table S6**. *n* represents the number of BPMs in the stack.

Next, we normalize the voltage to the number of BPMs in the stack, because the CO_2 regeneration occurs for each BPM, so when calculating the energy intensity, it should be on a per BPM unit basis.

$$\bar{V}_{stack} = \frac{(V_{anode} - V_{cathode} + n\bar{V}_{ohmic} + nV_{BPM})}{n} \quad \text{(S44)}$$

The energy intensity of the stack, E_{stack},can be calculated as

$$E_{stack} = F\frac{i_{stack}\bar{V}_{stack}}{i_{stack}\eta_{Coulomb}} \quad \text{(S45)}$$

where i_{stack} is the current density passed through the stack.

We assume HER and OER in acid and base, at the anode and cathode, respectively:

$$2H^+ + 2e^- \rightarrow H_2 |\ U_0 = 0\ V\ vs.RHE\ (pH = 0) \quad \text{(S46)}$$

$$4OH^- \rightarrow 2H_2O + 2O_2 + 2e^- |\ U_0 = 0.40\ V\ vs.RHE\ (pH = 14) \quad \text{(S47)}$$

Assuming 100 mV of overpotential to drive each reaction at 100 mA cm^{-2}, we determine $V_{anode} = 0.5\ V\ vs.\ RHE$ and $V_{cathode} = -0.1\ V\ vs.\ RHE$. Next, since we have found that thin buffer electrolyte layers (~10 μm) are sufficient to enable significant conversion of the fed (bi)carbonate, and high flow and thinner boundary layers enable better bubble management, a stack design with very thin electrolyte layers will likely be optimal for performance. Thus, we assume a conservative ohmic potential loss per unit ($\bar{V}_{ohmic}$) of 50 mV per unit. Using these values, normalized stack potentials and energy intensity can be calculated as follows for BPMs operating at 100 mA cm^{-2}.

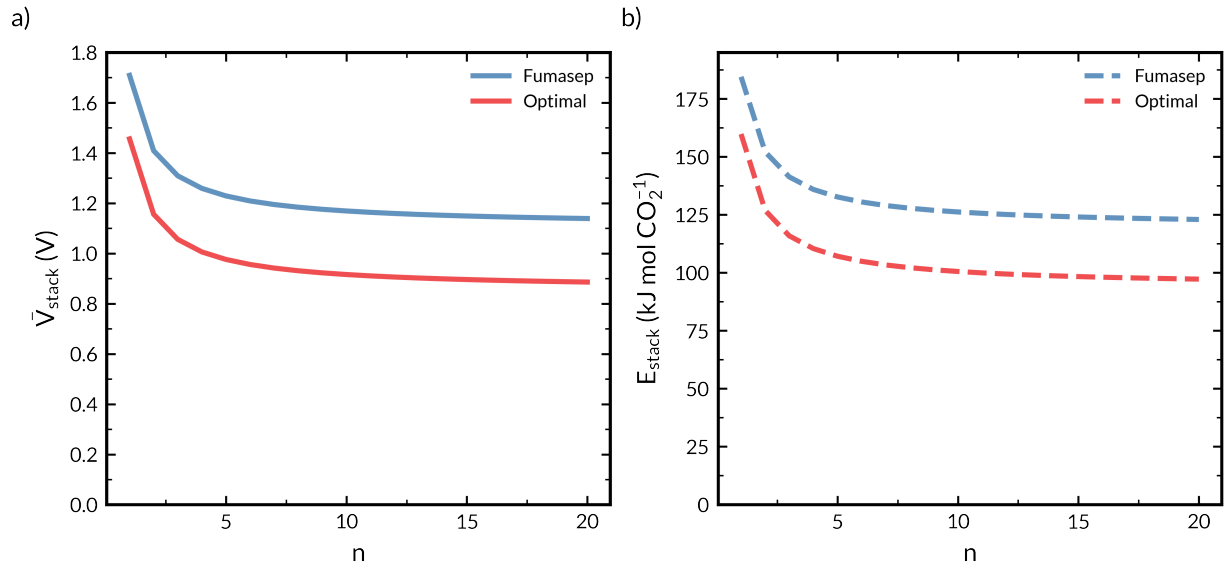

Figure S64: (a) Normalized stack potential and **(b)** Energy intensity of the stack as a function of number of BPMs in the BPM-ED stack.

S26. Nomenclature

Roman

a_i	Activity of species i
c_i	Concentration of species i (M)
D_i	Diffusivity of species i ($m^2\ s^{-1}$)
E	Electric field ($V\ m^{-1}$)
f_i	Activity coefficient of species i
F	Faraday constant ($C\ mol^{-1}$)
G	Gibbs free energy ($J\ mol^{-1}$)
IEC	Ion Exchange capacity ($mmol\ g^{-1}$)
k_B	Boltzmann constant ($J\ K^{-1}$)
K_n	Equilibrium constant in reaction n
k_n	Forward rate constant of reaction n ($mol\ m^{-3}\ s^{-1}$)
L	Length (m)
l_B	Bjerrum Length (m)
M_i	Molar mass of species i ($g\ mol^{-1}$)
N_i	Molar flux of species i ($mol\ m^{-2}\ s^{-1}$)
R	Ideal gas constant ($J\ mol^{-1}\ K^{-1}$)
$R_{B,i}$	Source term for species i ($mol\ m^{-3}\ s^{-1}$)
$s_{i,n}$	Stoichiometric coefficient of species i in reaction n
T	Temperature (K)
x	1-dimensional position variable (m)
z_i	Charge of ion i

Greek

β	Non-dimensional electric field scaling factor ($m\ V^{-1}$)
ε	Dielectric permittivity ($F\ m^{-1}$)
λ	Water content
μ	Chemical potential of species i ($J\ mol^{-1}$)
ξ	Species-membrane/Species-water diffusivity ratio
ρ	Density ($g\ cm^{-3}$)
σ	Dimensionless dissociation bond length
Φ	Electrostatic potential (V)
ε_k	Volume fraction of phase k

Subscript

char	Characteristic
eff	Effective
i	Species index
M	Value in membrane
w	Value in water

Superscript

0	Intrinsic value or standard state
E	Electric field dependence

Acronyms

aBL	Anolyte boundary layer
AEL	Anion exchange layer
BPM	Bipolar membrane
cBL	Catholyte boundary layer
CEL	Cation exchange layer
CL	Catalyst layer
WD	Water dissociation

S27. References

(1) Onsager, L.; Fuoss, R. M. Irreversible Processes in Electrolytes. Diffusion, Conductance, and Viscous Flow in Arbitrary Mixtures of Strong Electrolytes. *J. Phys. Chem.* **1932**, *36*, 2689–2778.

(2) Bui, J. C.; Corpus, K. R. M.; Bell, A. T.; Weber, A. Z. On the Nature of Field Enhanced Water Dissociation in Bipolar Membranes. *J. Phys. Chem. C* **2021**, *125* (45), 24974–24987.

(3) Lin, M.; Digdaya, I. A.; Xiang, C. Modeling the Electrochemical Behavior and Interfacial Junction Profiles of Bipolar Membranes at Solar Flux Relevant Operating Current Densities. *Sustain. Energy Fuels* **2021**, *5* (7), 2149–2158.

(4) Craig, N. P. Electrochemical Behavior of Bipolar Membranes. **2013**.

(5) Mareev, S. A.; Evdochenko, E.; Wessling, M.; Kozaderova, O. A.; Niftaliev, S. I.; Pismenskaya, N. D.; Nikonenko, V. V. A Comprehensive Mathematical Model of Water Splitting in Bipolar Membranes: Impact of the Spatial Distribution of Fixed Charges and Catalyst at Bipolar Junction. *J. Memb. Sci.* **2020**, *603*.

(6) Bui, J. C.; Digdaya, I.; Xiang, C.; Bell, A. T.; Weber, A. Z. Understanding Multi-Ion Transport Mechanisms in Bipolar Membranes. *ACS Appl. Mater. Interfaces* **2020**, *12* (47), 52509–52526.

(7) Lucas, É.; Bui, J. C.; Hwang, M.; Wang, K.; Bell, A. T.; Weber, A. Z.; Ardo, S.; Atwater, H. A.; Xiang, C. Asymmetric Bipolar Membrane for High Current Density Electrodialysis Operation with Exceptional Stability. *Chemrxiv* **2023**, 1–33.

(8) Grew, K. N.; Chiu, W. K. S. A Dusty Fluid Model for Predicting Hydroxyl Anion Conductivity in Alkaline Anion Exchange Membranes. *J. Electrochem. Soc.* **2010**, *157* (3), B327.

(9) Choi, P.; Jalani, N. H.; Datta, R. Thermodynamics and Proton Transport in Nafion II. Proton Diffusion Mechanisms and Conductivity. *J. Electrochem. Soc.* **2005**, *152* (3).

(10) Blommaert, M. A.; Aili, D.; Tufa, R. A.; Li, Q.; Smith, W. A.; Vermaas, D. A. Insights and Challenges for Applying Bipolar Membranes in Advanced Electrochemical Energy Systems. *ACS Energy Lett.* **2021**, *6*, 2539–2548.

(11) Strathmann, H.; Krol, J. J.; Rapp, H. J.; Eigenberger, G. Limiting Current Density and Water Dissociation in Bipolar Membranes. *J. Memb. Sci.* **1997**, *125* (1), 123–142.

(12) Krol, J. J.; Jansink, M.; Wessling, M.; Strathmann, H. Behaviour of Bipolar Membranes at High Current Density Water Diffusion Limitation. *Sep. Purif. Technol.* **1998**, *14* (1–3), 41–52.

(13) Crothers, A. R.; Darling, R. M.; Kusoglu, A.; Radke, C. J.; Weber, A. Z. Theory of Multicomponent Phenomena in Cation-Exchange Membranes: Part II. Transport Model and Validation. *J. Electrochem. Soc.* **2020**, *167* (1), 013548.

(14) Gerhardt, M. R.; Pant, L. M.; Bui, J. C. M.; Crothers, A. R.; Ehlinger, V. M.; Fornaciari, J. C.; Liu, J.; Weber, A. Z. Methods—Practices and Pitfalls in Voltage

Breakdown Analysis of Electrochemical Energy-Conversion Systems. *J. Electrochem. Soc.* **2021**.

(15) Newman, J.; Thomas-Alyea, K. E. *Electrochemical Systems*, 3rd ed.; John Wiley and Sons, Inc.: Hoboken, NJ, 2004.

(16) U.S. Geological Survey. PHREEQC (Version 3) - A Computer Program for Speciation, Batch-Reaction, One-Dimensional Transport, and Inverse Geochemical Calculations.

(17) Bui, J. C.; Kim, C.; Weber, A. Z.; Bell, A. T. Dynamic Boundary Layer Simulation of Pulsed CO 2 Electrolysis on a Copper Catalyst. *ACS Energy Lett.* **2021**, *6*, 1181–1188.

(18) Bui, J. C.; Lees, E. W.; Pant, L. M.; Zenyuk, I. V.; Bell, A. T.; Weber, A. Z. Continuum Modeling of Porous Electrodes for Electrochemical Synthesis. *Chem. Rev.* **2022**, *122* (12), 11022–11084.

(19) Bui, J. C.; Digdaya, I.; Xiang, C. X.; Bell, A. T.; Weber, A. Z. Understanding Multi-Ion Transport Mechanisms in Bipolar Membranes. *ACS Appl. Mater. Interfaces* **2020**, *12* (47), 52509–52526.

(20) Lu, Z.; Polizos, G.; Macdonald, D. D.; Manias, E. State of Water in Perfluorosulfonic Ionomer (Nafion 117) Proton Exchange Membranes. *J. Electrochem. Soc.* **2008**, *155* (2), B163.

(21) Pilson, M. E. Q. *Introduction to Chemistry of the Sea*, 2nd ed.; Cambridge University Press: Cambridge, UK, 1998.

(22) Bui, J. C.; Davis, J. T.; Esposito, D. V. 3D-Printed Electrodes for Membraneless Water Electrolysis. *Sustain. Energy Fuels* **2020**, No. 4, 213–225.

(23) Marin, D. H.; Perryman, J. T.; Hubert, M. A.; Lindquist, G. A.; Chen, L.; Aleman, A. M.; Kamat, G. A.; Niemann, V. A.; Stevens, M. B.; Regmi, Y. N.; Boettcher, S. W.; Nielander, A. C.; Jaramillo, T. F. Hydrogen Production with Seawater-Resilient Bipolar Membrane Electrolyzers. *Joule* **2023**, *7* (4), 765–781.

(24) Han, J. H.; Jwa, E.; Lee, H.; Kim, E. J.; Nam, J. Y.; Hwang, K. S.; Jeong, N.; Choi, J.; Kim, H.; Jeung, Y. C.; Chung, T. D. Direct Seawater Electrolysis via Synergistic Acidification by Inorganic Precipitation and Proton Flux from Bipolar Membrane. *Chem. Eng. J.* **2022**, *429* (April 2021), 132383.

(25) Oener, S. Z.; Twight, L. P.; Lindquist, G. A.; Boettcher, S. W. Thin Cation-Exchange Layers Enable High-Current-Density Bipolar Membrane Electrolyzers via Improved Water Transport. *ACS Energy Lett.* **2021**, *6* (1), 1–8.

(26) Petrov, K. V.; Bui, J. C.; Baumgartner, L.; Weng, L. C.; Dischinger, S. M.; Larson, D. M.; Miller, D. J.; Weber, A. Z.; Vermaas, D. A. Anion-Exchange Membranes with Internal Microchannels for Water Control in CO2 Electrolysis. *Sustain. Energy Fuels* **2022**, *6* (22), 5077–5088.

(27) Weber, A. Z.; Newman, J. Transport in Polymer-Electrolyte Membranes. *J. Electrochem. Soc.* **2004**, *151* (2), A311.

(28) Vermaas, D. A.; Wiegman, S.; Smith, W. A. Ion Transport Mechanisms in Bipolar

Membranes for (Photo)Electrochemical Water Splitting. *Sustain. Energy Fuels* **2018**, No. 9, 2006–2015.

(29) Kusoglu, A.; Weber, A. Z. New Insights into Perfluorinated Sulfonic-Acid Ionomers. *Chem. Rev.* **2017**, *117* (3), 987–1104.

(30) Luo, X.; Rojas-Carbonell, S.; Yan, Y.; Kusoglu, A. Structure-Transport Relationships of Poly(Aryl Piperidinium) Anion-Exchange Membranes: Eeffect of Anions and Hydration. *J. Memb. Sci.* **2020**, *598* (August 2019), 117680.

(31) Chen, L.; Oener, S. Z.; Fabrizio, K.; Boettcher, S. W. Design Principles for Water Dissociation Catalysts in High-Performance Bipolar Membranes. *Nat. Commun.* **2022**, *13*, 1–10.

(32) Mitchell, J. B.; Chen, L.; Langworthy, K.; Fabrizio, K.; Boettcher, S. W. Catalytic Proton-Hydroxide Recombination for Forward-Bias Bipolar Membranes. *ACS Energy Lett.* **2022**, *7* (11), 3967–3973.

(33) Park, H. B.; Kamcev, J.; Robeson, L. M.; Elimelech, M.; Freeman, B. D. Maximizing the Right Stuff: The Trade-off between Membrane Permeability and Selectivity. *Science (80-.).* **2017**, *356* (6343), 1138–1148.

(34) Powers, D.; Mondal, A. N.; Yang, Z.; Wycisk, R.; Kreidler, E.; Pintauro, P. N. Freestanding Bipolar Membranes with an Electrospun Junction for High Current Density Water Splitting. *ACS Appl. Mater. Interfaces* **2022**, *14* (31), 36092–36104.